Title
BRANCHING RATIOS OF REACTIONS OF n"" MESONS STOPPED IN HYDROGEN AND DEUTERIUM

Author
Ryan, James.

Publication Date
1962-05-01

UCRL-9884

UNIVERSITY OF CALIFORNIA

Lawrence Radiation Laboratory
Berkeley, California

Contract No. W-7405-eng-48

BRANCHING RATIOS OF REACTIONS OF π^- MESONS STOPPED IN HYDROGEN AND DEUTERIUM

James Ryan

(Thesis)

May, 1962

Printed in USA. Price $1.25. Available from the
Office of Technical Services
U. S. Department of Commerce
Washington 25, D.C.

DISCLAIMER

BRANCHING RATIOS OF REACTIONS OF π^- MESONS STOPPED IN HYDROGEN AND DEUTERIUM

Table of Contents

Table of Contents, Continued

ABSTRACT

The Panofsky ratio, $P = \omega(\pi^- + p \rightarrow \pi^0 + n)/\omega(\pi^- + p \rightarrow \gamma + n)$, and the branching ratio $S = \omega(\pi^- + d \rightarrow n + n)/\omega(\pi^- + d \rightarrow \gamma + n + n)$, have been measured by stopping π^- mesons in liquid hydrogen and liquid deuterium and detecting the gamma rays produced. A high resolution gamma-ray spectrometer of the 180-degree-focussing type was employed. Sixty-six Geiger tubes and nine scintillation counters were used in the spectrometer to define the electron-positron orbits, providing an intrinsic instrument resolution of 0.8%. The values obtained for the branching ratios are:

$$P = 1.51 \pm 0.04 \quad \text{and}$$

$$S = 3.16 \pm 0.10.$$

This value for P is in good agreement with that obtained in previous measurements while the value for S is significantly larger than previous results. With regard to the conventional phenomenological analysis of S-wave pion physics, the Panofsky ratio is in good agreement whereas the value obtained in this experiment for the branching ratio S is considerably larger than predicted.

I. INTRODUCTION AND PURPOSE

When a π^- meson comes to rest ($\beta < 0.01$) in liquid hydrogen, nuclear capture occurs in approximately 10^{-12} seconds through one of the following channels:

$$\pi^- + p \rightarrow \pi^o + n \qquad (1)$$
$$\pi^- + p \rightarrow \gamma + n \qquad (2)$$
$$\pi^- + p \rightarrow e^- + e^+ + n \qquad (3)$$

Reaction (1), mesic capture, produces a 0.41 Mev neutron and a π^o meson with $\beta = 0.21$. The lifetime for decay of the π^o is approximately 2×10^{-16} seconds and leads to one of the following final states:

$$n + \gamma + \gamma \qquad (1a)$$
$$n + \gamma + e^+ + e^- \qquad (1b)$$
$$n + e^+ + e^- + e^+ + e^- \qquad (1c)$$

The branching ratio of the internal conversion reaction (1b) to reaction (1a) has been calculated by Joseph[1] to be 0.00710. Due to motion of the π^o the gamma rays emitted are uniformly distributed in energy between 54.75 and 83.25 Mev.

Reaction (2), radiative capture, yields an 8.9 Mev neutron and a monoenergetic gamma ray of 129.4 Mev. Reaction (3) corresponds to internal conversion of this gamma ray. The branching ratio $\frac{(3)}{(2)}$ is calculated as 0.01196.[1]

It is customary to define the Panofsky ratio, P, as the branching ratio between the mesic capture and radiative capture reaction rates without regard for the low yield internal conversion processes, i.e. the ratio $\frac{(1)}{(2)}$, which in practice has generally meant $\frac{(1a)}{(2)}$. However, it is more appropriate to define as the ratio of the rate for all strongly interacting channels to the rate for all channels which are electromagnetic in origin[11], i.e.:

$$P = \frac{(1)}{(2)+(3)} = \frac{(1a)+(1b)}{(2)+(3)} . \qquad (4)$$

Since the manner of definition can lead to a difference of 1% in quoted value, we choose to give our results for P in terms of (4) above.

When π^- mesons come to rest in deuterium the following nuclear reactions occur:

$$\pi^- + d \rightarrow n + n \qquad (5)$$
$$\pi^- + d \rightarrow n + n + \gamma \qquad (6)$$
$$\pi^- + d \rightarrow n + n + \pi^0 \qquad (7)$$

Reaction (5) yields monoenergetic neutrons of 67.5 Mev. The radiative capture reaction (6) produces gamma rays with a distribution of energies ranging from 0 to 131.5 Mev which is peaked near the high energy end as a result of the n-n interaction. Reaction (7), mesic capture, gives a π^0 meson with β ranging from 0 to 0.12 which results in gamma rays distributed in energy between 60 and 76 Mev.

In their original experiment Panofsky et al.[2] stopped π^- mesons in both hydrogen and deuterium and detected the nuclear gamma rays with a pair spectrometer. In addition to measuring the Panofsky ratio, they also obtained values for the deuterium ratios S and R, defined as:

$$S = \frac{\omega\,(\pi^- + d \rightarrow n + n)}{\omega\,(\pi^- + d \rightarrow n + n + \gamma)} \text{ and} \qquad (8)$$

$$R = \frac{\omega\,(\pi^- + d \rightarrow n + n + \pi^0)}{\omega\,(\pi^- + d \rightarrow n + n + \gamma)} \, . \qquad (9)$$

Since this initial work several additional measurements of the Panofsky ratio have been published.[3-11] A list of these, the method employed and the values obtained are given in Table 1. Previous measurements of S and R[2,12,13,14] are listed in Table 2.

Anderson and Fermi[15] first pointed out that the Panofsky ratio serves as a connecting link between reactions in pion-nucleon scattering and pion photoproduction. Brueckner, Serber, and Watson[16] completed the scheme outlined in Figure 1 by relating the deuterium ratio S to pion production in nucleon-nucleon collisions and to the other interactions. In the figure, reactions denoted with the subscript b indicate bound state capture while those which have been measured at positive energies and extrapolated to threshold are underlined. These relationships provide a means of checking the internal consistency of a large body of knowledge in low energy pion physics.

For the scheme outlined in Figure 1 to be applicable it is necessary to know for the bound state reactions from what angular momentum states nuclear capture occurs. In the past most analyses have been made

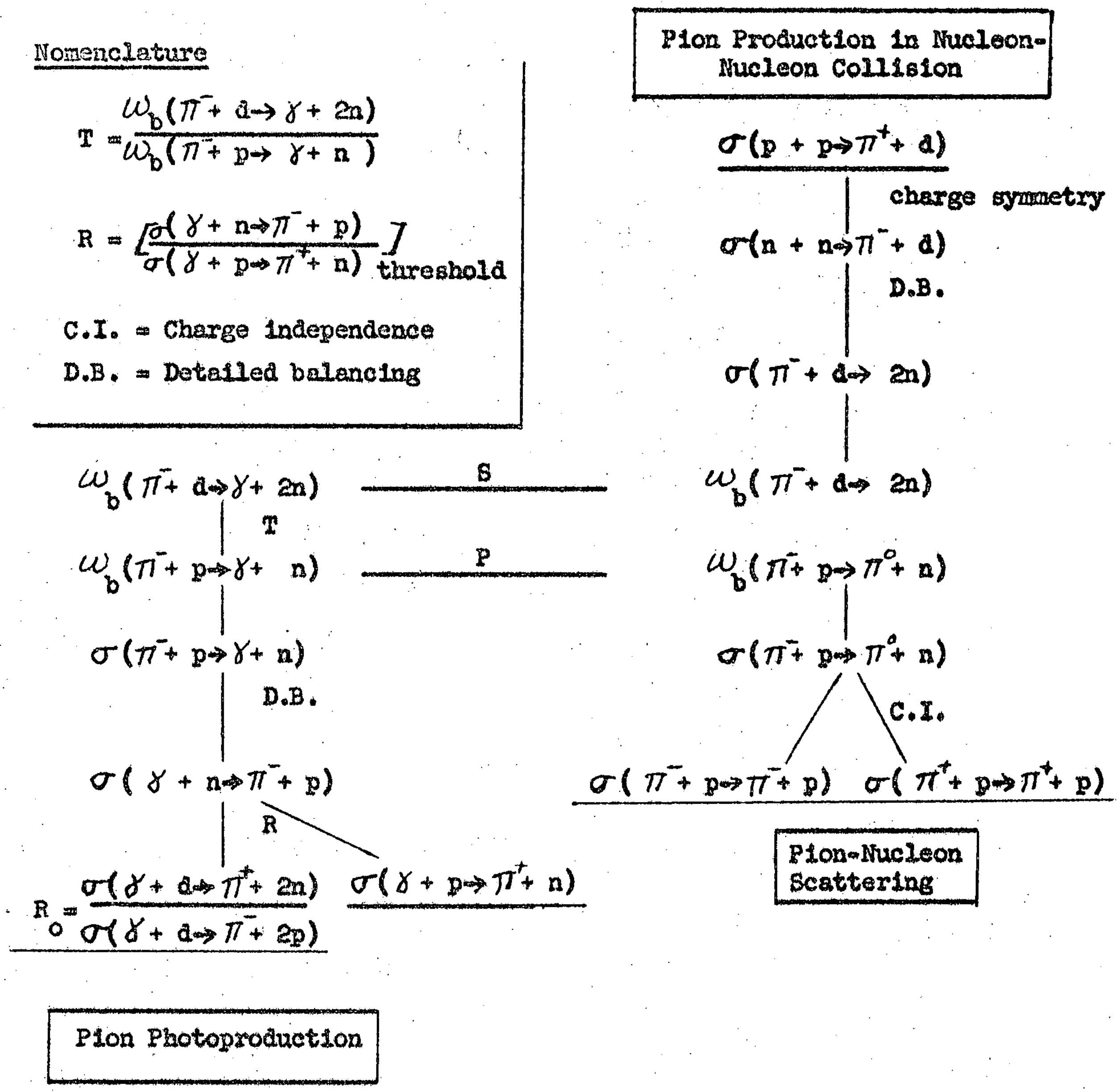

Fig. 1. Phenomenological outline of S-wave pion physics.

on the basis of capture from the 1S state of the mesic atom. The mechanism for formation of the mesic atom was assumed to be as described by Wightman.[17] However, a recent measurement of the nuclear capture time in hydrogen by Fields et al.[18] indicates that this previous description of the formation process is not completely correct and that capture does not take place from the 1S orbit. Although at the present time no direct experimental measurement has defined the states from which capture does occur, recent work by G. A. Snow,[19] Russell and Shaw,[20] and Day, Snow, and Sucher[21] offers an explanation of the problem in terms of S-wave capture from higher n states of the mesic atom.

If it is assumed that capture does occur predominately from S states, the ratios P and S can be expressed as follows:

$$P = \frac{4\pi}{9R}\,\frac{v_o}{q}\,\frac{(1+\mu/M)^2}{(1+\mu/2M)^2}\,\frac{(a_3-a_1)^2}{\sigma(\gamma+p\rightarrow\pi^++n)} \qquad (10)$$

$$S = \frac{1}{3T'R}\,\frac{1+\mu/M}{1+\mu/2M}\,\frac{Mq}{q^D}\,\frac{\sigma(p+p\rightarrow\pi^++d)}{\sigma(\gamma+p\rightarrow\pi^++n)} \qquad (11)$$

Here μ and M are the pion and nucleon rest masses, a_3 and a_1 are the S-wave scattering lengths for isotopic spin states 3/2 and 1/2, respectively, v_o is the π^o velocity relative to the neutron for the charge exchange reaction in hydrogen, while q and q^D are incident c.m. π^- momenta for the reactions in hydrogen and deuterium. In addition, $T' = T\,|\phi_H(0)|^2/|\phi_D(0)|^2$ where $\phi_H(0)$ and $\phi_D(0)$ are the wave functions for the respective hydrogen and deuterium mesic atom states from which capture occurs, both evaluated at the position of the nucleus. T and R are defined in Figure 1. These equations follow from the relationships in Figure 1 and have been discussed previously.[4,5,15,16] A simple derivation is presented in Appendix A.

Since Anderson and Fermi first published their paper, discrepancies between the calculated Panofsky ratio, Equation (10), and the measured value have stimulated a large amount of work both experimental and theoretical. At various times several different suggestions were offered to explain these discrepancies, including violation of charge independence in the pion-nucleon system[22] and even the existence of a new particle.[23] However, due largely to the theoretical work of Baldin,[23] Cini, Gatto, Goldwasser, and Ruderman,[24] and Hamilton and Woodcock[25] plus more precise determinations of the Panofsky ratio, no serious discrepancies now seem to exist.

The chain of reactions in deuterium shown in Figure 1 provides an independent check on the results in hydrogen. Because of the relatively large uncertainties in previous measurements of S and in knowledge of the ratio T, this check has not been very useful.

In this experiment we have remeasured both the Panofsky ratio P and the deuterium ratio S. Together with a recent more accurate evaluation of T[26] all three legs of the scheme outlined in Figure 1 are now believed to be known with comparable accuracy. In Table 3 the calculated and measured values of P and S are compared.

II. EXPERIMENTAL METHOD

Uncertainty in previous measurements of the Panofsky ratio has been due to statistics as well as the inability of the detection apparatus to adequately resolve the low and high energy gamma rays involved. Considering this and the fact that we also wished to determine the spectrum of gamma rays from the deuterium reaction with good resolution, a gamma-ray pair spectrometer was selected. The spectrometer is of the 180-degree-focussing type and is discussed in detail in Section III.

Panofsky Ratio

If a large number of π^- mesons stop in hydrogen, the Panofsky ratio is equal to the ratio of the number of mesic capture reactions to the number of radiative capture reactions which occur. Let $N_{\gamma 1}$ and $N_{\gamma 2}$ be the number of gamma rays from each of these reactions, respectively, which strike the converter of the spectrometer. If no losses occur in the target then the Panofsky ratio can be written as

$$P = \frac{N_{\gamma 1}}{2N_{\gamma 2}} \tag{12}$$

where the 2 compensates for the two gamma rays produced in the mesic capture reaction. With the pair spectrometer these numbers are determined by detecting the electron-positron pairs produced in the converter.

Detection efficiency versus energy for the pair spectrometer is triangular in shape with maximum efficiency at the mean energy E and with energy width $(1 \pm 1/2)E$. Due to these conditions the Panofsky ratio can be measured with optimum efficiency by using two different mean energy settings of the spectrometer, one corresponding to the energy of the radiative capture gamma ray, the other to the mid-point energy of the distribution of mesic capture gamma rays. A special characteristic of the 180° design in regard to electron scattering (see paragraph III-D) makes this quite attractive since accurate calculations of absolute scattering losses are not necessary if the converter thicknesses are appropriately chosen.

For a fixed magnetic field setting the present spectrometer is capable of detecting the gamma rays from both reactions but with reduced efficiency.

It was decided to make two independent measurements, one with a single fixed field, the other using two different fields. For the three field settings the converter thicknesses were chosen such that scattering losses were equalized. Thereby, an absolute comparison of the gamma-ray yield at different magnetic fields for each of the two reactions provided a rigorous check of the pair spectrometer.

Deuterium Ratio S

If a large number, N, of π^- mesons stop in hydrogen and the same number in deuterium, we can write

$$N = N_1(\pi^- + p \rightarrow \pi^0 + n) + N_2(\pi^- + p \rightarrow \gamma + n)$$
$$= N_3(\pi^- + d \rightarrow n + n) + N_4(\pi^- + d \rightarrow n + n + \gamma) \qquad (13)$$

where N_1, N_2, N_3, and N_4 are the numbers of interactions which occur in the respective channels. (The small contributions from internal conversion processes are neglected.) Since $P = \frac{N_1}{N_2}$ and $S = \frac{N_3}{N_4}$, Equation (13) can be restated as:

$$PN_2 + N_2 = SN_4 + N_4 \qquad \text{or}$$

$$S = (1 + P)\frac{N_2}{N_4} - 1 \quad . \qquad (14)$$

Since there is one gamma ray emitted in each of these radiative capture reactions, then, if $N_{\gamma 2}$ and $N_{\gamma 4}$ are the number of gamma rays incident on the spectrometer converter from the respective reactions, S can be expressed as

$$S = (1 + P)\frac{N_{\gamma 2}}{N_{\gamma 4}} - 1. \qquad (15)$$

Hence, this ratio can be determined using the measured value for the Panofsky ratio and counting only the radiative capture gamma rays from hydrogen and deuterium.

III. EXPERIMENTAL EQUIPMENT

A. Equipment Set-up

Arrangement of the experimental equipment in the meson beam cave of the 184-inch Synchro-cyclotron is shown in Figure 2. The meson beam is produced in a Be target bombarded in the cyclotron. Leaving the vacuum tank by a thin window, the beam passes through an 8-inch diameter quadrapole doublet and an 8-foot diameter iron collimating wheel with a 5-inch square aperture. The beam is reduced in energy by passing through an aluminum degrader, the thickness of which is chosen so that the mesons stop in the liquid hydrogen or deuterium flask.

A fraction of the gamma rays, produced by π^- mesons interacting in the liquid hydrogen, pair produce in the converter of the pair spectrometer, M_2, and the resulting electron-positron pairs are detected.

Lead bricks forming a 6-inch square collimating hole near the hydrogen target shield the converter from view of all portions of the target except the flask. The small magnet M_1 is employed to sweep away charged particles which might otherwise enter the spectrometer entrance channel. In addition, a 4-foot thick concrete and steel shielding wall is located between the hydrogen target and the spectrometer in order to reduce background at the spectrometer.

B. Meson Beam Monitoring and Optimization

Two separate beam monitoring systems were used. One, an ion chamber, was located near the cyclotron vacuum tank inside the shielding wall and the ion current was continuously monitored. The other, a gamma-ray telescope, was located below the hydrogen target. Refer to Figure 4. A coincidence between scintillation counters 2, 3, and 4 combined with no count in counter 1 indicated pair conversion of a gamma ray in the 1/4" lead plate. The counting rate is proportional to the rate of stopping mesons.

The rate of mesons stopping in the target was maximized by suitably locating the internal cyclotron target, selecting optimum coil currents in the focussing quadrapole, and choosing the optimum aluminum degrader thickness. See Figure 2. Counting rates of the gamma-ray telescope described in the preceding paragraph were monitored during this procedure.

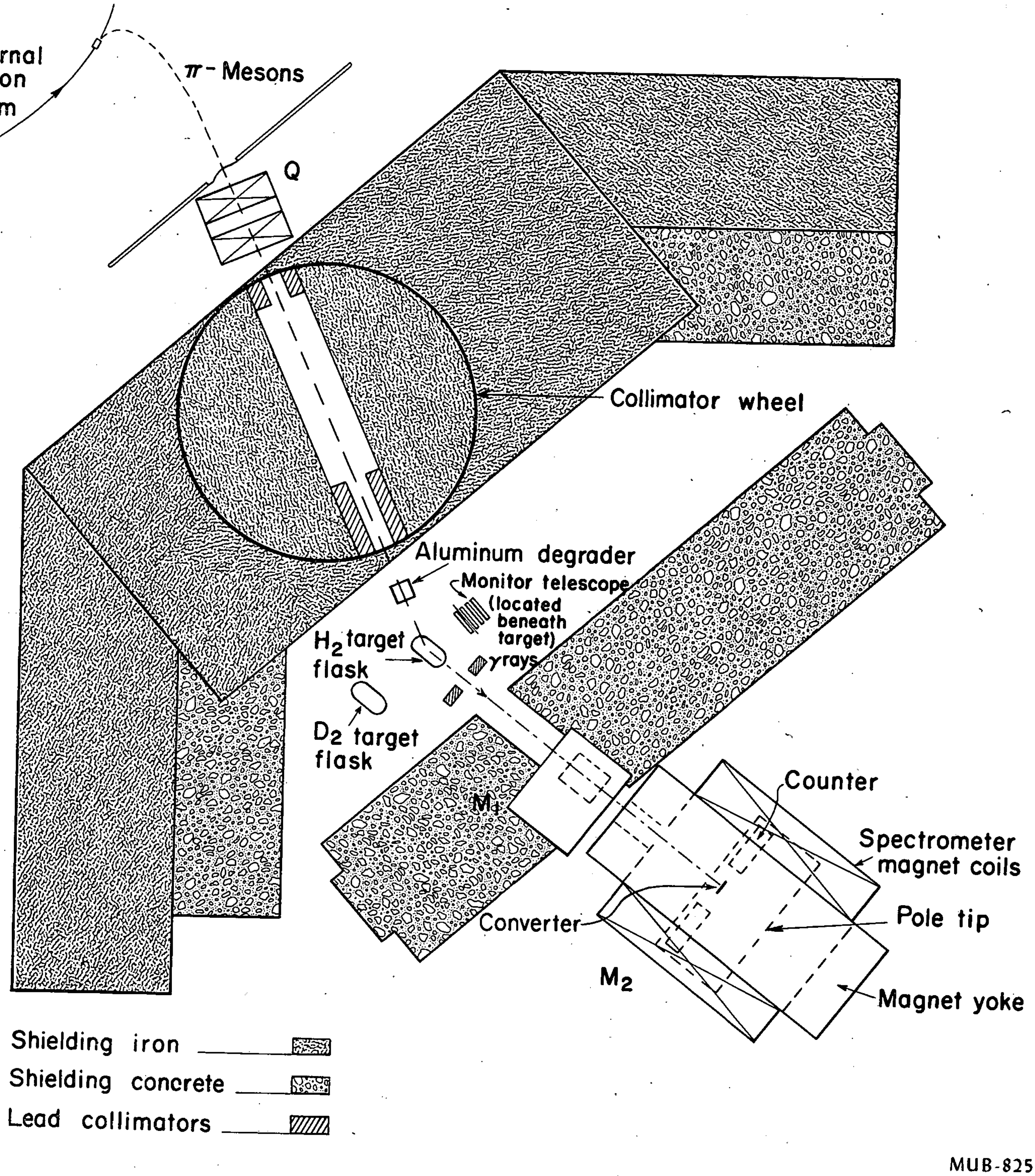

Fig. 2. Equipment set-up in the meson-beam cave of the 184" Synchrocyclotron.

Figure 3 shows the measured gamma-ray telescope counting rate versus degrader thickness with hydrogen in the target. The large peak in the curve is due to gamma rays produced by nuclear reactions of stopped π^- mesons. The aluminum degrader thickness determined from this curve (5-5/8 inches) was used throughout the experiment.

C. Hydrogen and Deuterium Targets

A schematic drawing of the targets and target supporting stand is shown in Figure 4. The targets were rigidly mounted on a carriage on which four flanged wheels engaged with a set of parallel rails near the top of the supporting stand. The carriage was moveable by hand to allow positioning either of the target flasks in the beam path. Mechanical stops and clamps were used to hold the carriage securely in place.

A schematic diagram showing the target flask, heat shield, and outer vacuum jacket is shown in Figure 5. Both the hydrogen and deuterium targets are of identical design. The flask shape is cylindrical with a 6-inch diameter and 10-inch average length. It is contoured on each end for strength and fabricated from 0.010 inch mylar. Ends of the heat shield are covered by 0.00025 inch aluminized mylar while the outer vacuum jacket is spun aluminum 0.035 inches thick. Not shown in the figure are 3/8 inch stainless steel fill tubes which are rigidly connected to the flask by contoured washers and nuts.

Although the lead collimator shields the pair spectrometer from gamma rays originating in the aluminum degrader, the copper heat shield, and other portions of the H_2 target, a section of the hydrogen fill lines is 'visible'. However, since only a few percent of the incoming π^- meson beam intercept these parts and also since all gamma rays detected with the target empty can be attributed to reactions in the residual H_2 gas, no appreciable influence on the ratios being measured seems possible.

In order to guard against contamination of the liquid hydrogen, transfer of the hydrogen from dewar to target was accomplished using hydrogen gas under pressure.

D. The Gamma ray Pair Spectrometer

A top view of the spectrometer with the upper half of the electromagnet removed is shown in Figure 6. In this drawing the aluminum rack

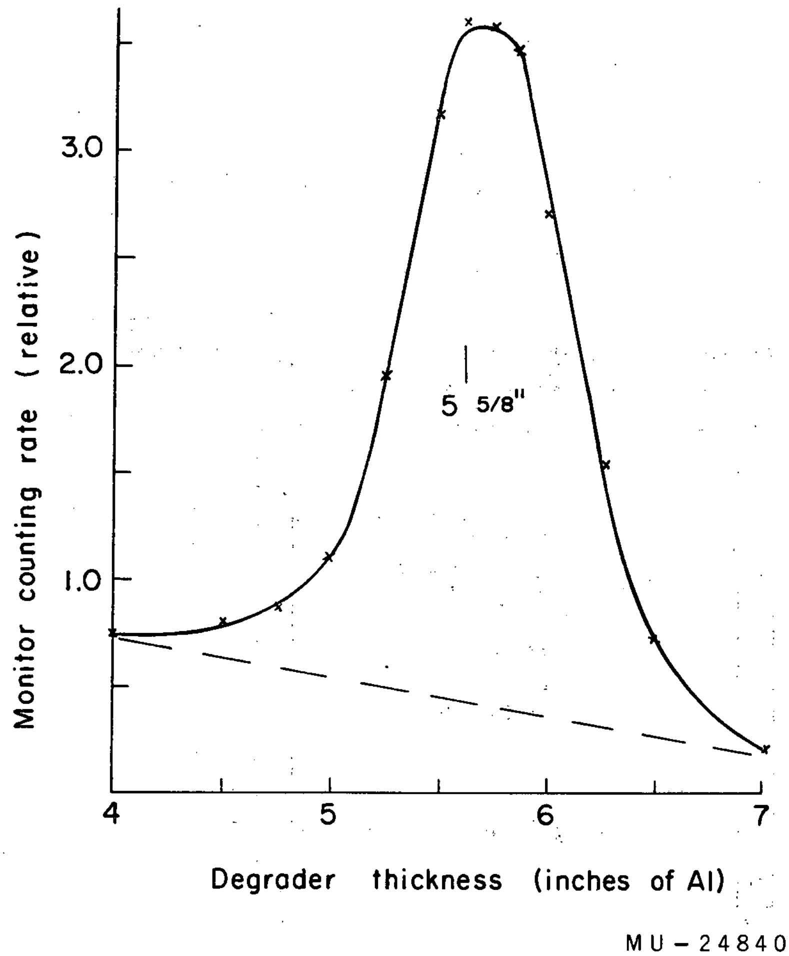

Fig. 3. Monitor telescope counting rate vs energy degrader thickness.

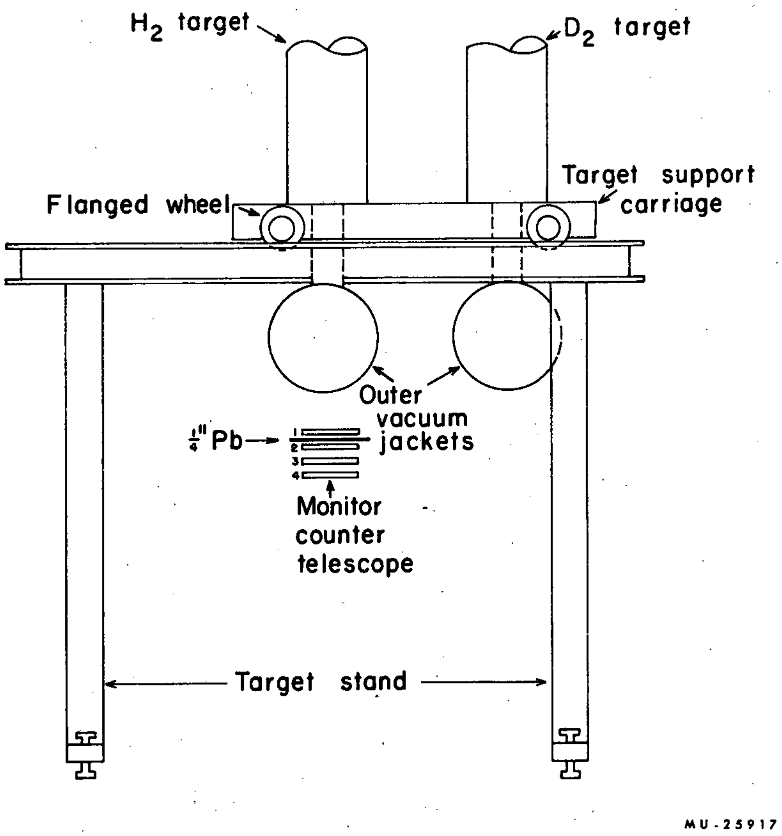

Fig. 4. Schematic drawing showing H_2 and D_2 targets and supporting stand. (Monitor telescope also shown.)

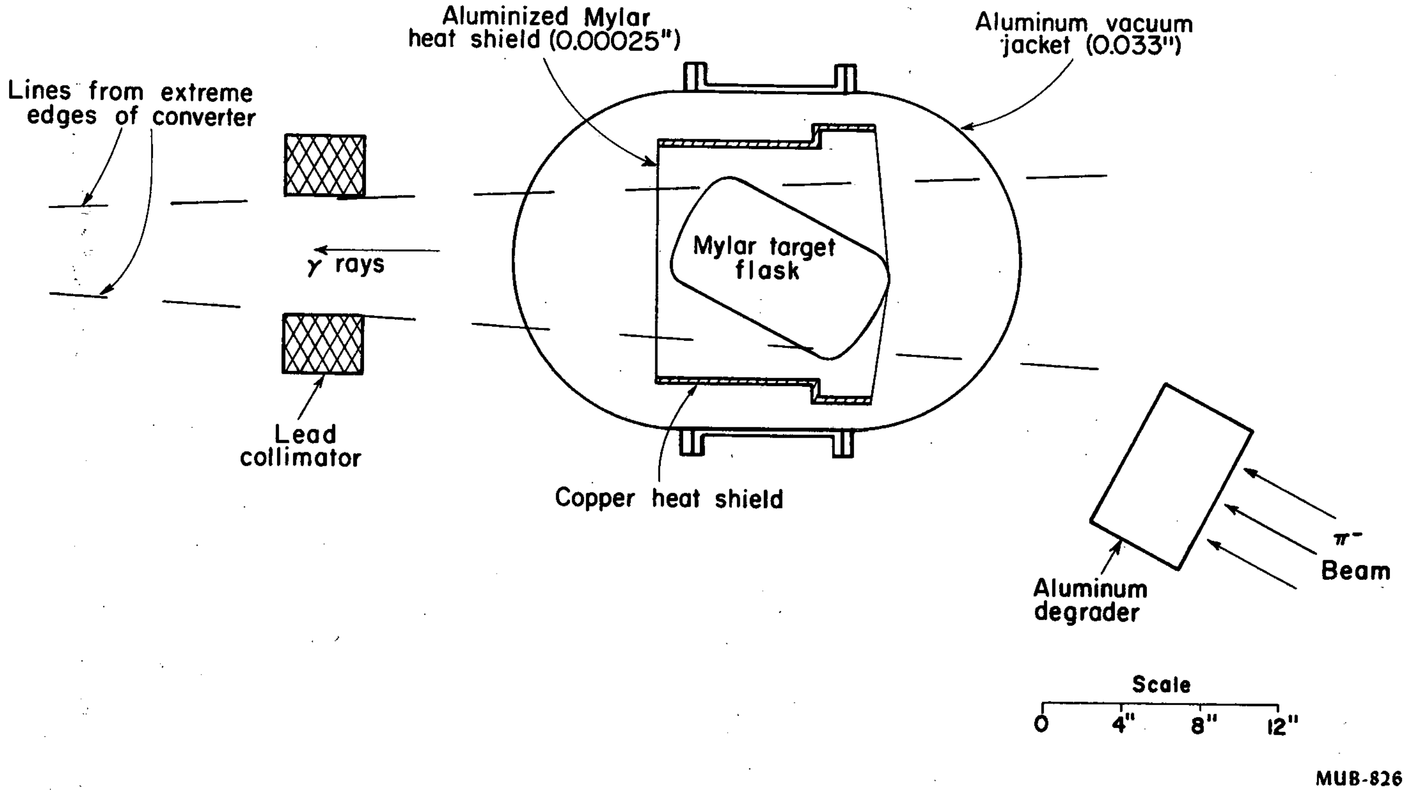

Fig. 5. Diagram showing target and beam configuration.

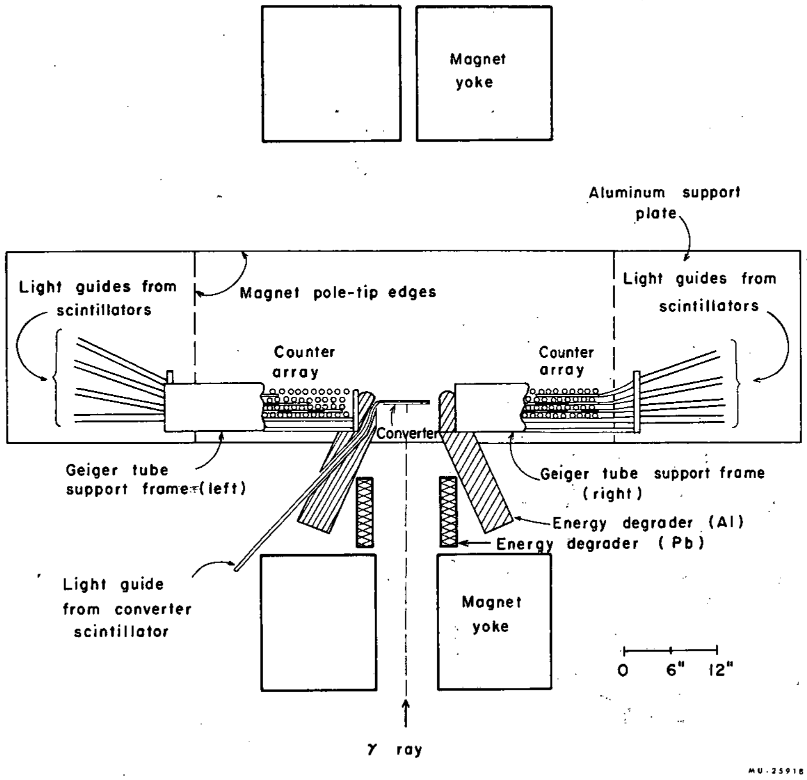

Fig. 6. Top view of spectrometer with upper half of electro-
magnet yoke removed.

which supports the Geiger tubes is cut away to afford an unobstructed view of the detecting array.

Gamma rays enter the spectrometer through a 6-inch x 7-inch hole in the electromagnet yoke and pair produce in the converter. The electron and positron produced are turned in a circular path by a uniform magnetic field perpendicular to the plane of the drawing and detected at the 180° position. An array of 33 Geiger tubes on each side of the converter plus nine scintillation counters served to detect the particles and to determine the sum of their energies.

The distance between the centers of the detection region on both sides of the converter is 32 inches. As will be described later, overlap of the Geiger tubes gives a 0.25-inch channel width. Together these dimensions define an intrinsic instrument resolution of 0.8%.

1. General Features of the 180° Design

The principles of the 180° pair spectrometer were first discussed by Walker and McDaniel[29] and applied to an instrument with an energy range of 5 to 40 Mev. Later, Kuehner, Merrison, and Tornabene[6] used this type of design in a previous measurement of the Panofsky ratio.

The important characteristics of the 180° design are described in the following paragraphs:

Energy determination and lateral width focussing. For a particle of charge e and momentum p moving in a uniform magnetic field B, the equation of motion is

$$\frac{Be}{c} = \frac{p}{\rho} \tag{16}$$

where ρ is the radius of curvature and c the velocity of light. For a relativistic electron $p \approx E$ and hence,

$$\rho = \frac{pc}{Be} = \frac{E}{Be} \quad . \tag{17}$$

Now if an electron and positron of total energy E^- and E^+, respectively, are produced in the converter, we can write

$$2(\rho^- + \rho^+) = \frac{2}{Be}(E^- + E^+)$$

or

$$E^- + E^+ = \frac{Be}{2}\ 2(\rho^- + \rho^+) \tag{18}$$

Therefore, the total electron-positron pair energy is proportional to the distance between orbits at the 180° position and independent of the horizontal position of pair creation in the converter. This latter property is termed lateral width focussing.

<u>180° focussing</u>. Various factors cause the pair members to emerge from the converter with angular displacements from the normal. In the spectrometer described here multiple scattering is most important with minor contribution due to angular effects and the pair creation process. In the 180° design horizontal displacement of the pair members at the focus line due to their angular displacements at the converter are minimized because of focussing to first order in the angle.

<u>Energy independence of scattering losses</u>. If the projected scattering angle on leaving the converter is sufficiently large, an electron will not intercept the detectors at the 180° position. This will be referred to as 'scattering out' or 'scattering loss'. If α' is the rms projected scattering angle and t the converter thickness, α' can be written as

$$\alpha' = C \frac{f(t)}{E} \tag{19}$$

where C is a constant and the function f(t) is defined in Appendix B. Now the orbital path length for an electron moving from converter to detector is $\pi\rho$ and hence the vertical displacement h at the detector for an electron with angle α' is

$$h = \pi\rho\alpha' = \pi \frac{E}{Be} \frac{C\,f(t)}{E} = \frac{C\pi}{e} \frac{f(t)}{B} \quad . \tag{20}$$

Hence, the vertical displacement is independent of E, and therefore the 'scattering losses' are independent of E. Equation (20) also indicates that for different values of B the thickness t can be appropriately chosen such that these losses are equalized.

2. <u>The Magnetic Field</u>

It is an obvious calculational advantage for a pair spectrometer to have a uniform magnetic field such that particle orbits are circular arcs. Also, because of limitations on the range of gamma ray energies detectable with such an instrument (in this case $(1 \pm 1/2)$ E for a mean energy E), it is necessary to operate at various magnetic field settings if measurement of a broad gamma-ray spectrum is desired. For a measurement of the Panofsky ratio the detection efficiency is optimized if measurements are made at two mean energy settings corresponding to the radiative capture gamma-ray peak and the central energy of the π^{o} gamma ray distribution.

For these reasons a program of magnetic field measurements and shimming the spectrometer magnet was undertaken. The pole tip and shim configuration adopted is shown in Fig. 7. Thin pole tip surface shims, not shown in the figure, were used in the deuterium ratio measurement to provide a more uniform field.

The magnetic field settings B used in this experiment are:

B(gauss)	Application
5,538	Panofsky ratio
8,235	Panofsky ratio
11,013	Panofsky ratio
10,500	Deuterium ratio

Magnetic field contours for the magnet at these field settings are shown in Figures 8, 9, and 10 where the values given represent the field averaged over a 5-inch deep region centered about the median plane.

For the least uniform field, B = 11,013 gauss, calculations indicated that the maximum energy shift due to field variations amounts to < 0.25%. This has been confirmed by comparing the position of the radiative capture line for B = 10,500 and B = 11,013 gauss.

3. Converters

A converter assembly is shown in Fig. 11. The lead converter is mounted on a 0.060-inch lucite backing with plastic tape. Small lucite clamps mounted on the top surface of a 0.060-inch aluminum plate rigidly support the converter perpendicular to the plate. Slots in a set of parallel guide rails accept the edges of the aluminum plate while a position stop determines the desired location of the front edge of the plate. With this arrangement the converter could be located to within 0.015 inch of the desired location and converter assemblies could be rapidly interchanged.

Besides the lead and lucite backing, the converter scintillation counter also forms part of the converter system. However, the effective thickness for pair production in the converter counter is not known. The manner in which the data is treated to account for this is discussed in paragraph VI-C.

Characteristics and applications of the various converters used in this experiment are described in Table 4.

4. Counters

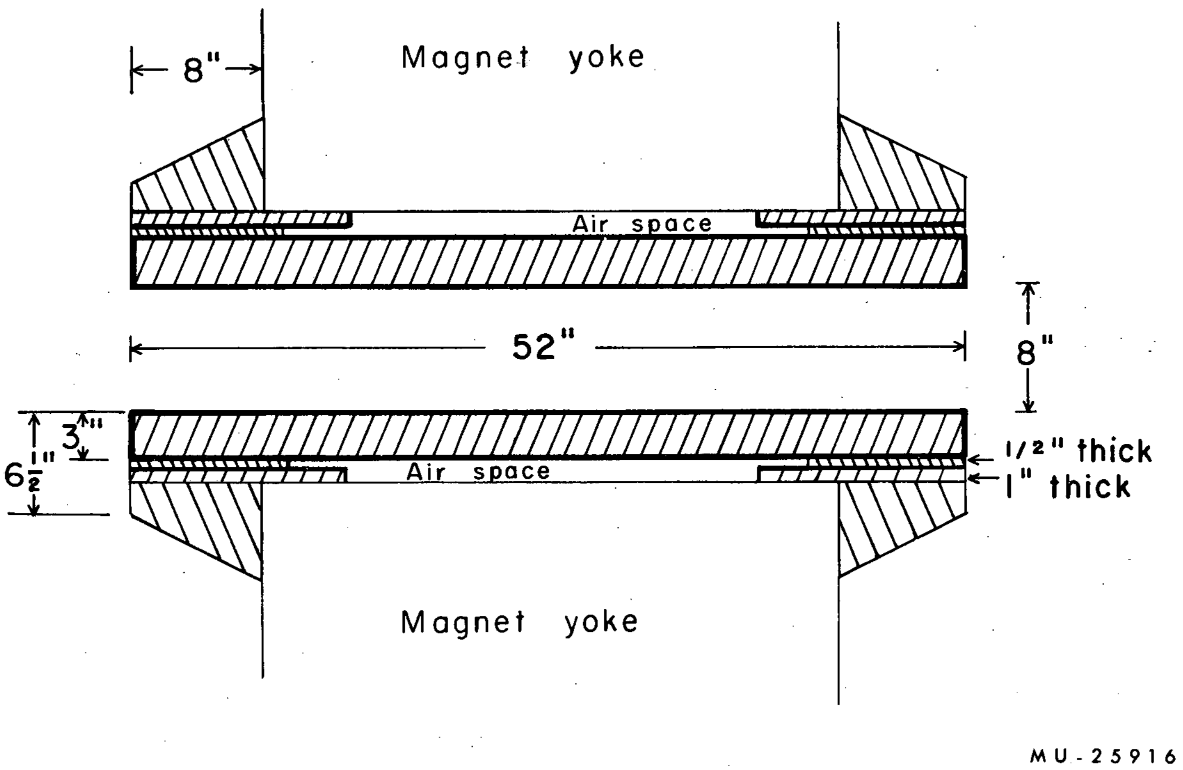

Fig. 7. Spectrometer pole tip and shim configuration.

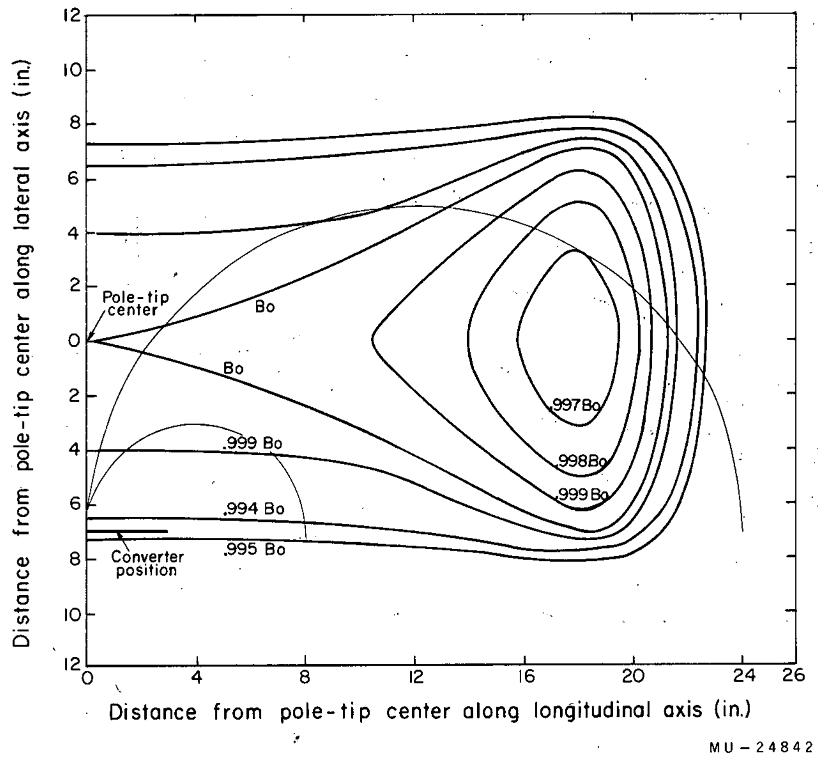

Fig. 8. Magnetic field contours for central field $B_o = 5538$ gauss.

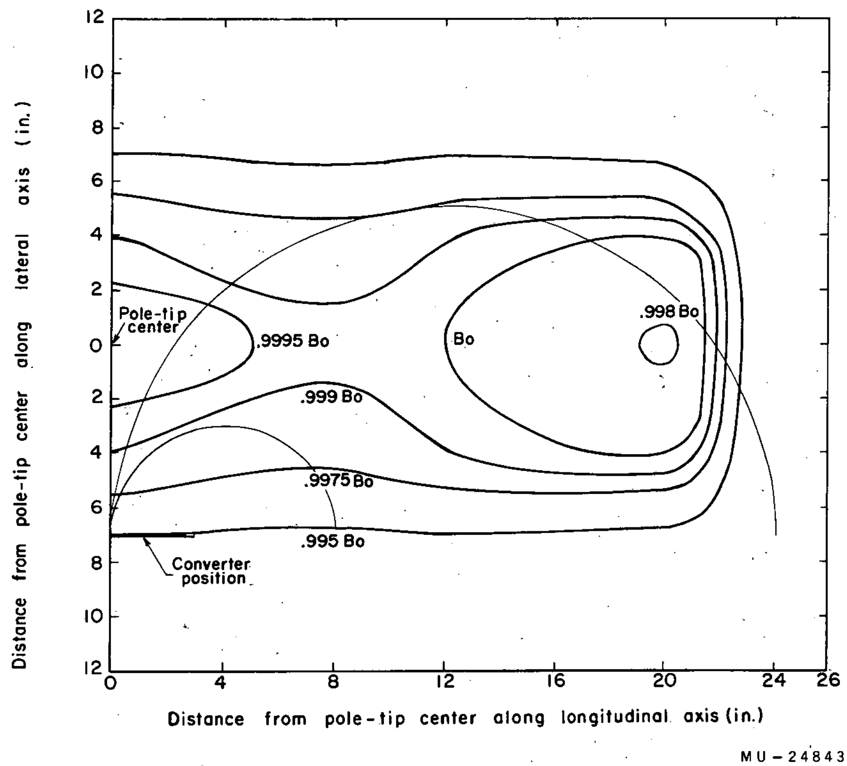

Fig. 9. Magnetic field contours for central field B_o = 10500 gauss.

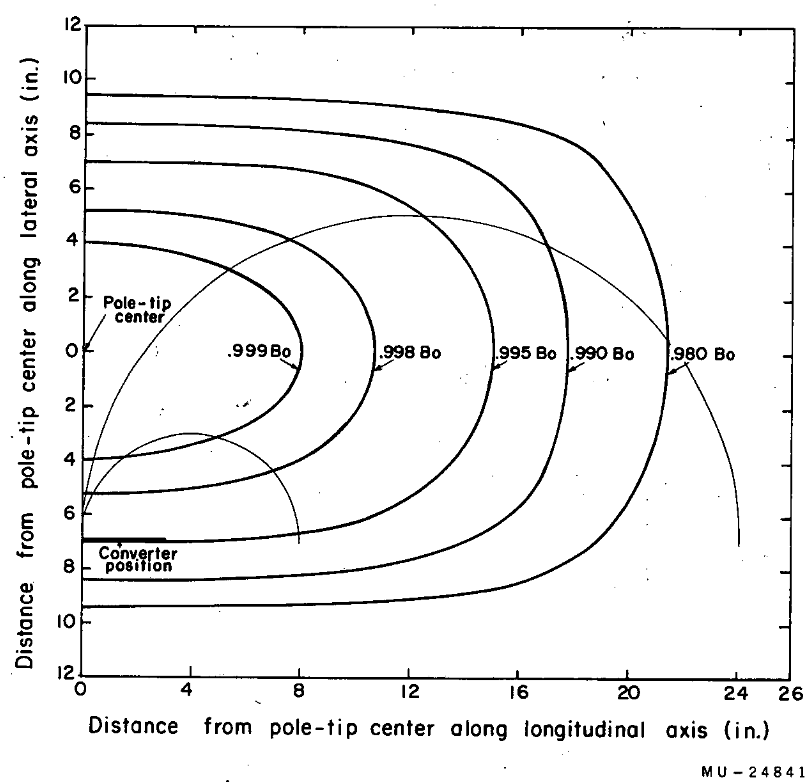

Fig. 10. Magnetic field contours for central field B_o = 11013 gauss.

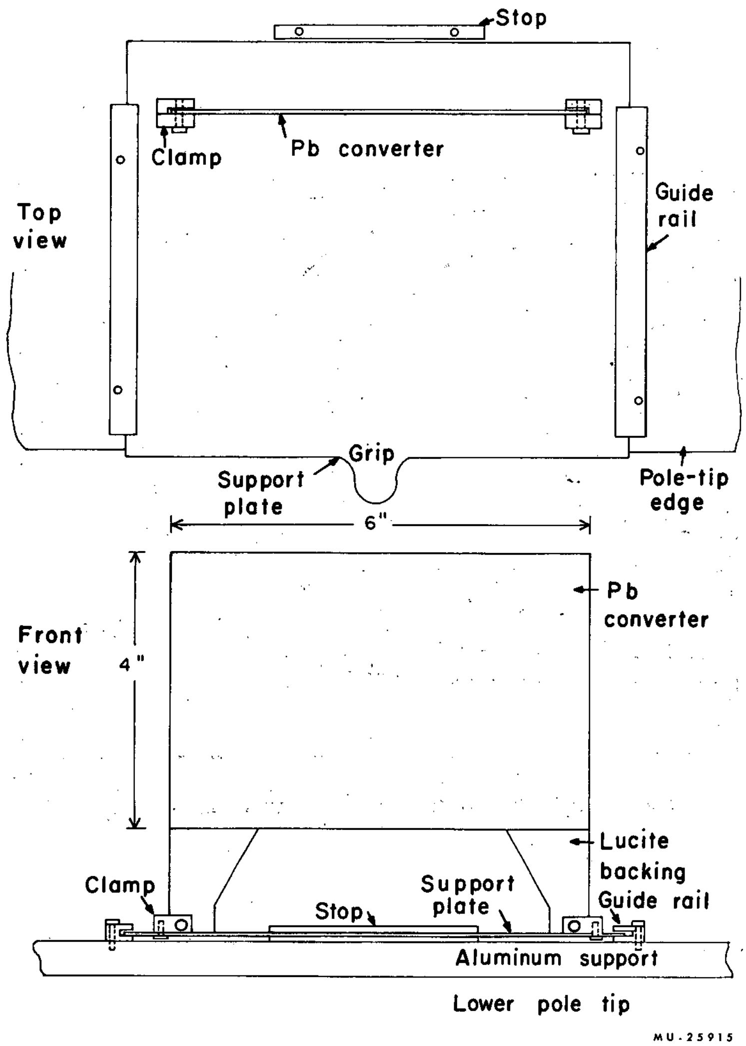

Fig. 11. Converter assembly.

The counter detection system consisted of 66 Geiger tubes and 9 scintillation counters arranged as shown in Figure 12. A coincidence between the gate counters (scintillators 1, 2-N, and 3P) indicates the detection of an electron-positron pair created in the converter. The total energy of the pair is determined by those Geiger tubes and scintillation counters, 4-N through 9-P, which fire in coincidence with the gate counters. The scintillation counters served as a check on the Geiger tube system and helped to define events when extra Geiger tubes fired.

Geiger tube arrangement. The Geiger tubes employed (Victoreen type 1B85) are cylindrical in shape with a 0.750-inch diameter outer aluminum shell of thickness 0.007 inches. A fine 0.002-inch wire along the axis of the cylinder forms the anode.

The present tube arrangement has been used previously.[30] By overlapping tubes and requiring a coincidence for the overlap channels, a channel width of 0.250 inches is provided. In order to increase the active area of the channels, pairs of Geiger tubes were arranged parallel end to end to provide a total active length of nearly 5 inches. A side view of the counter array is shown in Figure 13. Vertical overlap was employed to compensate for the reduced efficiency near the tube end. The positions of the tubes were known to within 0.015 inch.

Identically numbered tubes in Figure 12 define a pair of parallel tubes which form a part of the same energy channels and are connected electrically to the same lead. Each tube number N identifies the radius ρ of an electron orbit which passes through the tube center and the center of the converter, perpendicular to it. For the left bank (electron side) $\rho^- = \frac{48-N^-}{4}$ and for the right bank (positron side) $\rho^+ = \frac{N^+-48}{4}$. Hence, the total distance $2(\rho^- + \rho^+)$ between a pair of electron and positron channels, which is related to the total pair energy by Equation (18), is just

$$2(\rho^- + \rho^+) = \frac{N^+-N^-}{2} = \frac{2}{Be}\,(E^+ + E^-) \tag{21}$$

For the overlap channels, N^+ and N^- refer to the average of the numbers identifying the two overlapped tubes.

Scintillation counters. Dimensions of the nine scintillation counters are given in Table 5. Counters 2-N and 3-P are composed of tapered pieces of plastic scintillator and lucite bonded together with Epon to form a uniform 0.500-inch thick strip. The piece of scintillator ranged in

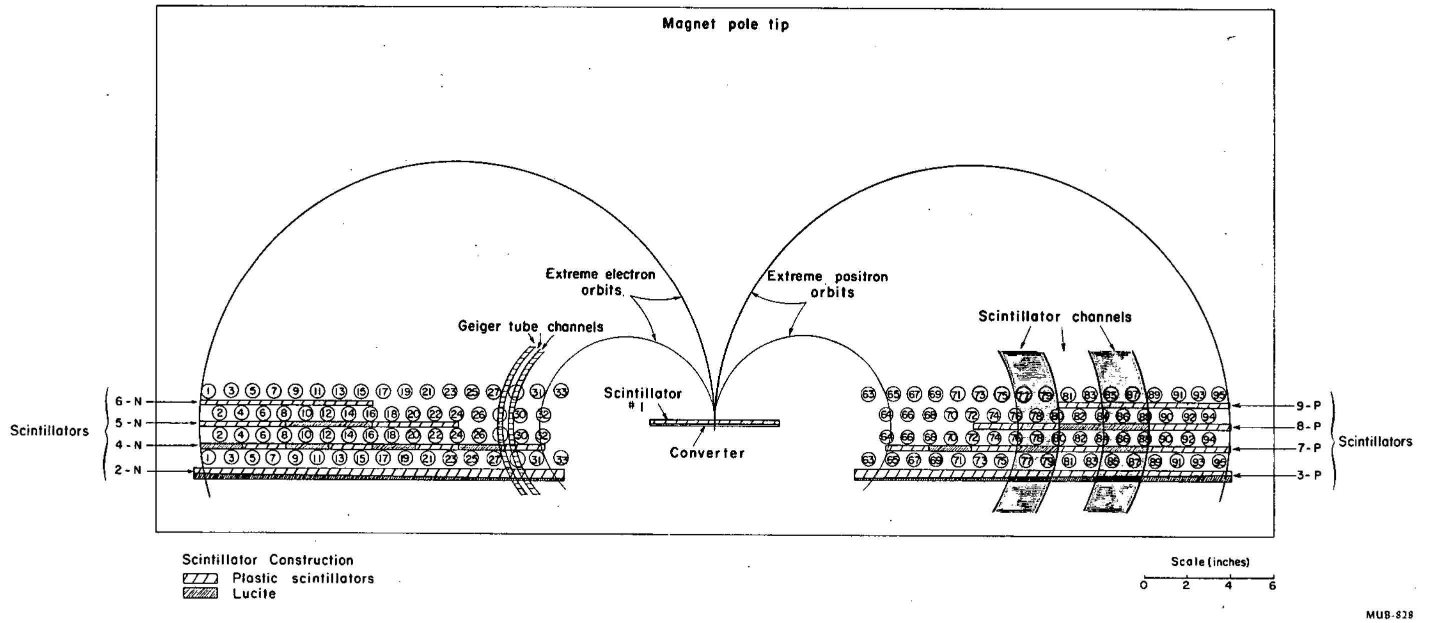

Fig. 12. Schematic drawing showing counter locations and Geiger tube numbering system.

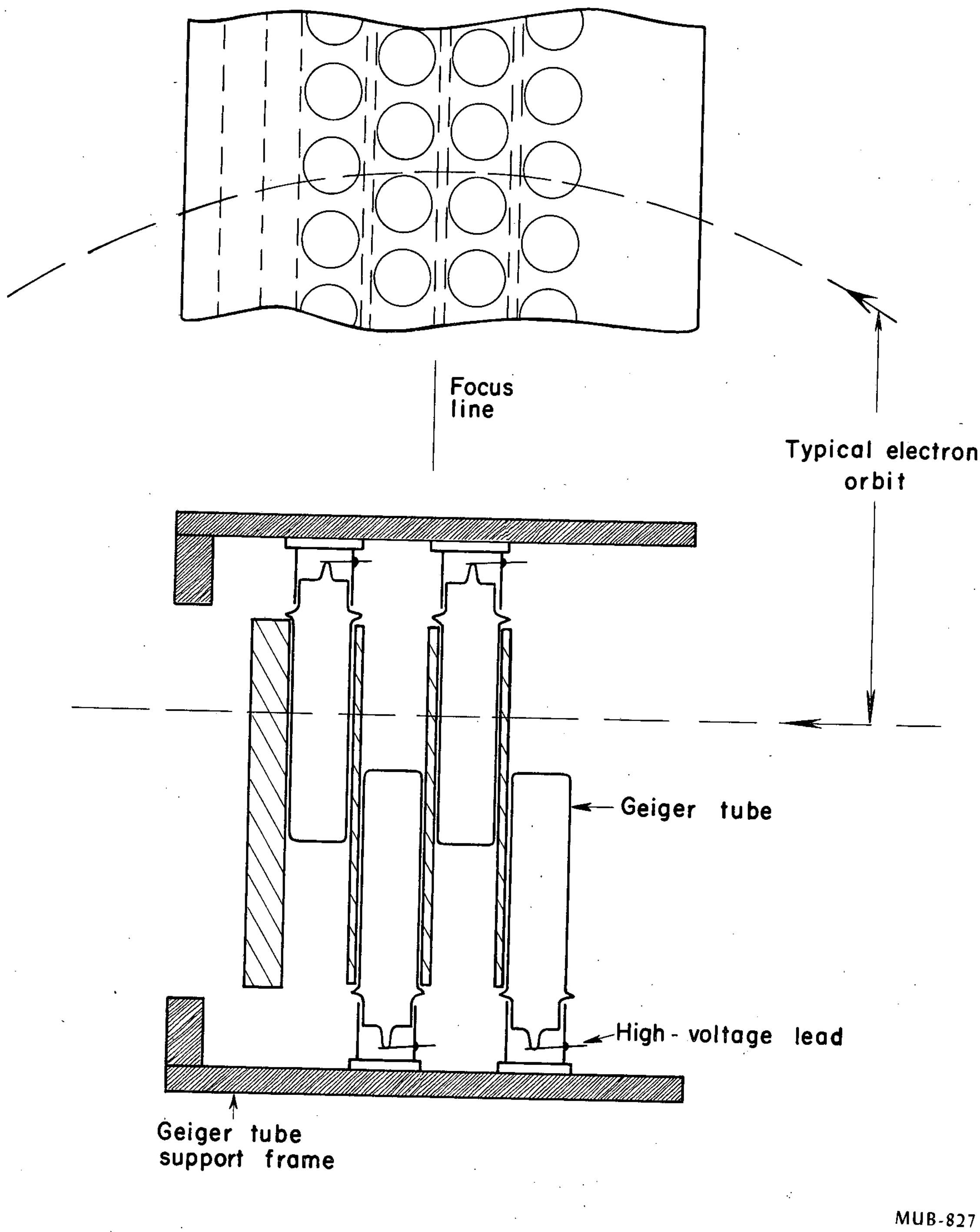

Fig. 13. Side view of counter array.

thickness from 0.25 inches at the end closest to the phototube to 0.45 inches at the opposite end. This design was incorporated to reduce the variation in pulse height with distance from the phototube and hence to insure that the detection efficiency was independent of electron energy.

Counters 4-N through 9-P form a complete separate system for defining the energy channels, with a resolution of 6%. However, the usefulness of this system was limited due to the relatively large efficiency (5 to 10%) for detecting Cerenkov radiation in the lucite strips.

Counter Efficiency. The rms variation in efficiency of the Geiger tubes used in the present experiment has been determined to be approximately 4%. The absolute efficiency as determined from the results of the present experiment is between 85 and 90%. Calculations indicate that the absolute efficiency should be nearly 100%; however, tube end effects may cause this difference.

By observing which channel scintillation counters fire when specific Geiger channels fire for the present set-up, it was determined that the efficiency for each scintillator channel (Refer to Figure 12.) was > 98%.

E. Electronics

A schematic drawing showing the electronics and related data recording instrumentation is shown in Figure 14.

A coincidence event (B, C, D, $\bar{\bar{E}}$) in the coincidence unit W-1 signifies a gamma ray has actuated the gamma-ray monitor telescope. This counting rate is monitored by scalers S-1(a) and S-1(b).

The function of the remaining circuitry is to detect and indicate photographically those Geiger tubes and those scintillation counters, 4-N through 9-P, which fire simultaneously with the three gate counters (1, 2-N, and 3-P). Detection of a coincidence between the gate counters in the fast coincidence unit W-3 triggers the discriminator SW-2. The fast output pulse actuates the gate generator G and also serves as one input to each of the 2-fold coincidence circuits W-4 through W-9.

Relative time delays in the system are adjusted so that, if any of the spectrometer channel counters, 4-N through 9-P, fire simultaneously with a coincidence of the gate counters, the corresponding coincidence units are triggered. These 2-fold coincidence events provide inputs to corresponding units of the "amplifier and pulse generator". Each of the 64 pair of parallel Geiger tubes is also connected to the input of one of these units.

A 20-volt, 5-μsec pulse from the gate generator, G, provides

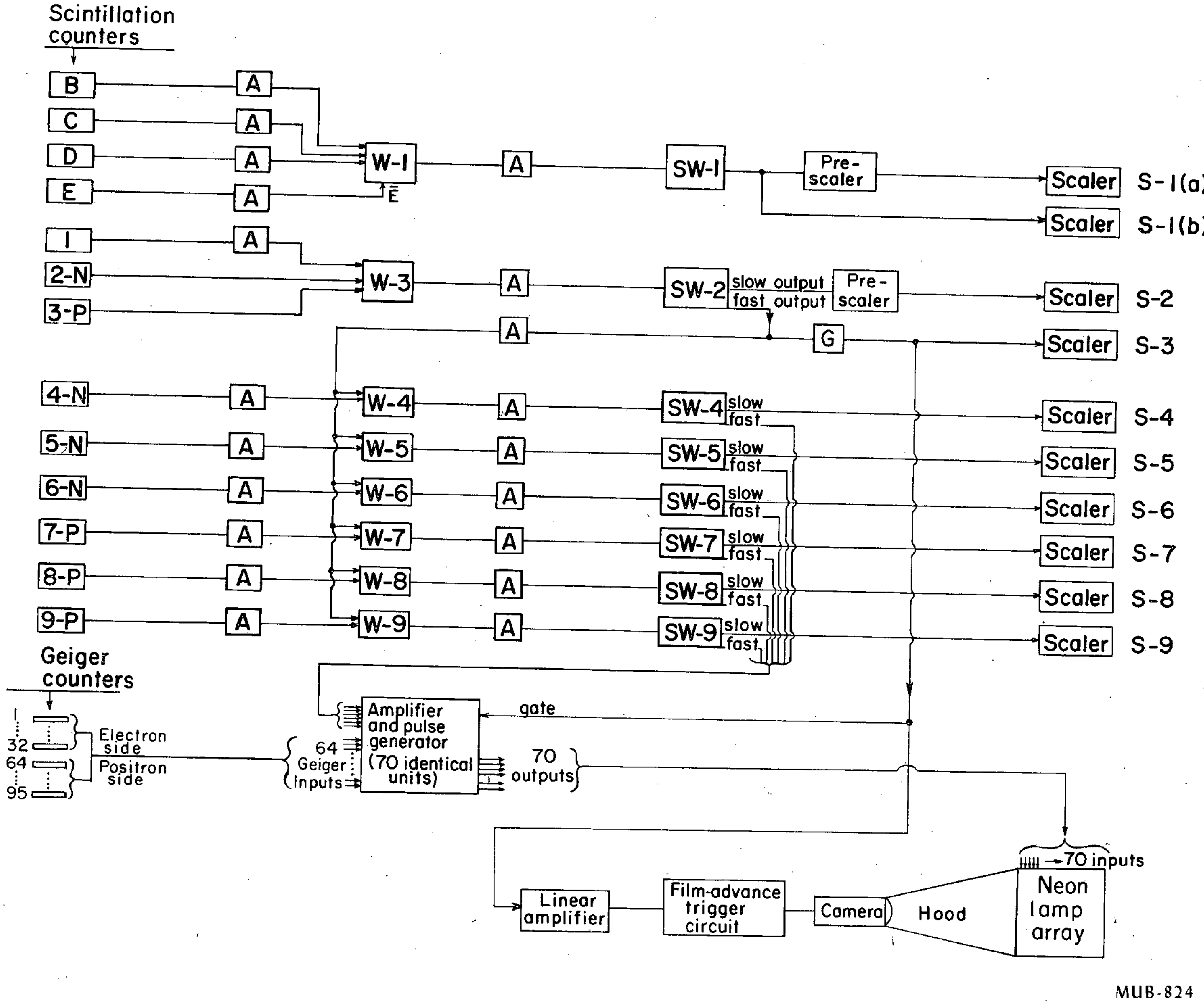

Fig. 14. Schematic drawing of the electronics and related data recording circuitry.

a slow coincidence between the gate counters and the channel defining counters in the "amplifier and pulse generator" units. A neon lamp is located in the output circuit of each unit. These lamps, when fired, indicate coincidence events and are photographically recorded.

The camera is a 35 mm Dumont type--modified to include an automatic film advance mechanism which is actuated by the gate pulse. Low intensity lights within the hood insured firing of the neon lamps when voltage was applied.

IV. EXPERIMENTAL PROCEDURE

Throughout the Panofsky ratio measurement the hydrogen target was clamped firmly in position. Cyclotron runs were made with various combinations of spectrometer converters and magnetic fields as indicated in Table 6. Panofsky ratios I and II refer to the two independent measurements performed as described in Section II, one utilizing a fixed magnetic field (II) and the other, two different fields (I). The runs with converter out determined the effect of the converter counter. Additional background measurements not indicated in the table were made with the converters both in and out but with the hydrogen removed from the flask. In order to help cancel systematic monitoring and background effects due to cyclotron operation a large number of individual runs were performed (130) alternating between the various magnetic field and converter combinations.

During measurement of the deuterium ratio S, runs with the hydrogen and deuterium targets were alternated. Nearly 20 one-hour runs were performed with each target. Magnetic field and converter combinations are shown in the table.

Frequent checks were made to ensure that the equipment was operating properly. All magnet currents and counter voltages were inspected every few hours. A closed circuit T.V. system permitted continuous monitoring of the hydrogen and deuterium target gauges. Similarly, visual presentation on a wall recorder of the output from the ion chamber monitor provided a continuous check on the cyclotron beam. In addition, the equipment was pulsed through several times during the experiment to make sure the timing had not changed or components had not failed.

Gamma-ray Yield vs Hydrogen Density

In order to correct for the difference in stopping power between the liquid hydrogen and deuterium, a measurement of gamma-ray yield vs. hydrogen density was performed. Changes in density were made by altering the pressure in the hydrogen flask. The minimum and maximum pressures attained were 3 psia and 30 psia, corresponding to a change of hydrogen density from 67 to 75 gm/liter. Values of density were determined by temperature measurements.

A copper-constantan thermocouple was used for the temperature measurements. One junction was located near the bottom of the hydrogen target while the reference junction was located in a liquid N_2 bath.

Voltage measurements were made with a Leed's and Northrup K-2 potentiometer. With this system the temperature could be determined to within 0.2 of a degree.

The test equipment used is shown in Figure 15. To acquire pressures above atmospheric the reservoir-flask system was closed off and the pressure allowed to rise. A relief valve set for 15 psig was provided to retain the pressure at a set value until temperature equilibrium was established. However, because of the slow rate of pressure increase, approximate temperature equilibrium was constantly maintained; hence measurements were made at several different pressures. Measurements consisted of simultaneous recordings of the gamma-ray monitor rate and the thermocouple voltage. For pressures below atmospheric the vacuum pump was connected directly to the hydrogen system. Measurements were performed as before for several pressures below atmospheric.

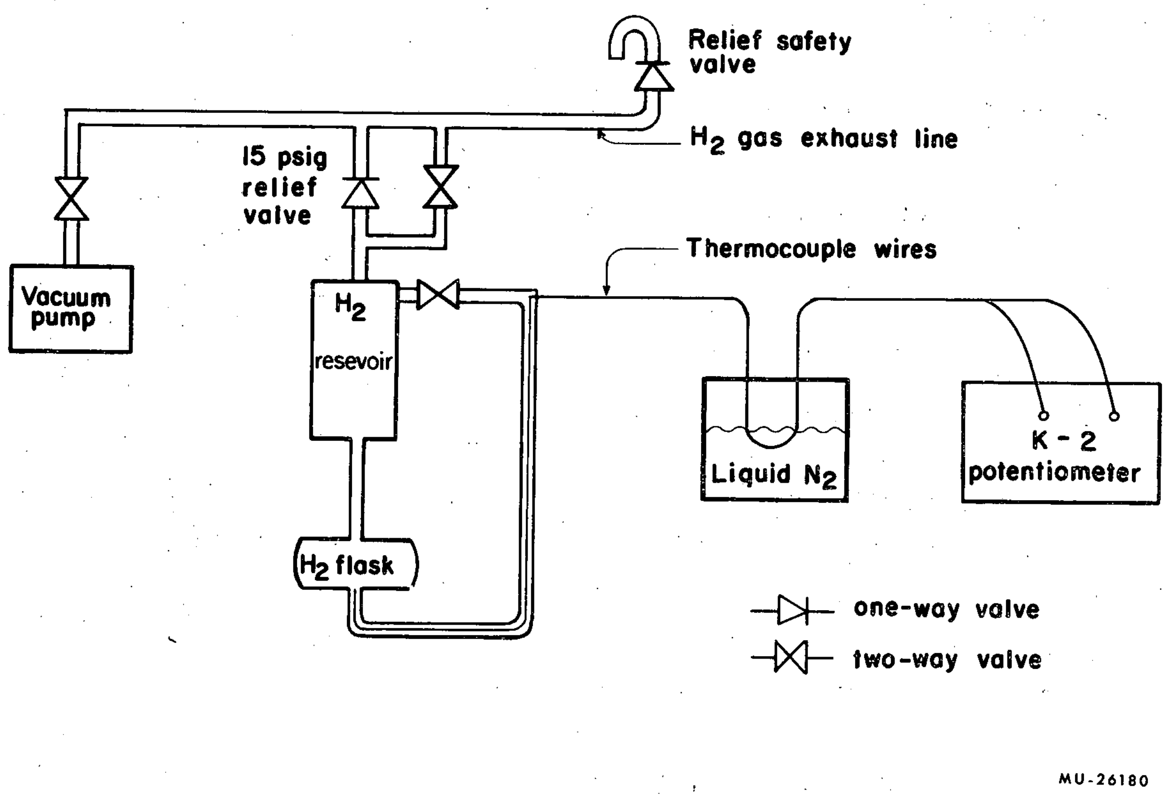

Fig. 15. Test equipment for hydrogen pressure test.

V. SPECTROMETER RESOLUTION AND DETECTION EFFICIENCY

Assume a gamma ray selected at random from a spectrum with energy distribution $I(E_\gamma)$ is incident on a converter of thickness T. Then the probability that a pair is produced and detected with total energy between E and E+ Δ E can be written as

$$P(E)\ \Delta E = \gamma(T)\ S(T,B) \int_{E_\gamma}^{E_\gamma} I(E_\gamma)\ r(E_\gamma, E) dE_\gamma\ \Delta E \quad \text{or} \qquad (22)$$

$$P(E)\ \Delta E = \gamma(T)\ S(T,B) \int I(E_\gamma) R\ (E_\gamma, E) dE_\gamma\ \epsilon(E)\ \Delta E \qquad (23)$$

where $\gamma(T)$ is the probability for pair production in the converter averaged over the spectrum of incident energies, S(T,B) is the probability that the vertical positions for both particles at the 180° point of their orbits are within the detector vertical limits, $r(E_\gamma, E)$ and $R(E_\gamma, E)$ are resolution functions, and $\epsilon(E)$ is defined as the lateral detection efficiency. The integration extends over all gamma-ray energies occurring in the distribution $I(E_\gamma)$. These equations are derived in Appendix C. The function $r(E_\gamma, E)$ describes the energy distribution of pairs for which both particles enter the detector region, while $R(E_\gamma, E)$ gives the complete energy distribution of pairs emerging from the converter. The efficiency $\epsilon(E)$ compensates for this difference and specifies the fraction of pairs with total energy E for which both particles enter the lateral limits of the detectors. $\epsilon(E)$ can be written for a fixed E_γ as

$$\epsilon(E) = \frac{r(E_\gamma, E)}{R(E_\gamma, E)} \qquad (24)$$

Due to the counter geometry and the thin converters employed in the present experiment $\epsilon(E)$ can be determined to within a few percent of its true value by geometry considerations alone.

The Resolution Function $R(E_\gamma, E)$

This function is defined as

$$R(E_\gamma, E) = \int^{E_o^-} p(E_\gamma, E_o^-) \int^{T} W(E_\gamma, t, B) \int^{E_1^-} F^-(E_\gamma, t, E_o^-, E_1^-)$$

$$\times\ F^+(E_\gamma - E_o^-, t, E - E_1^-)\ dE_1^-\ dt\ dE_o^- \quad , \qquad (25)$$

where the integrations extend over all values of the initial and final electron energies, E_0^- and E_1^-, and for which $\int_0^{E_\gamma} R(E_\gamma, E)dE = 1$. The function $p(E_\gamma, E_0^-)$ denotes the distribution of electron energies occurring in pair production and is shown in Figure 16 for a gamma-ray energy of 129 Mev. The function $W(E_\gamma, T, B)$ serves to weight slices of the converter with respect to pair production yield and to scattering losses. For given initial particle energies and position in the converter the functions F^- and F^+ describe the distribution in final electron and positron energies, E_1^- and $E-E_1^-$, upon leaving the converter. These latter functions include contributions to the energy loss due to bremsstrahlung (or radiation straggling) and ionization as well as the line broadening due to the Geiger tube channel width. In the calculation of the resolution these three effects have been treated separately and the resulting distributions folded together. For the channel width contribution this procedure is exact since the energy width of all channels is the same due to the uniform magnetic field. Separate treatment of the radiation and ionization effects is also a good approximation since the ionization energy loss for relativistic electrons is nearly independent of energy while the radiation losses change very little over a range of particle energies comparable to the average ionization loss in the converters used.

The channel width distribution was calculated by folding together two uniform distributions both of energy width equal to a geiger channel, one corresponding to the electron side of the spectrometer, the other to the positron side. The result of this fold is an equilateral triangle with base width equal to the sum of the channel widths and is shown in Figure 17 for a magnetic field setting of 11,013 gauss.

For ionization energy losses the Landau[31] distribution was used with the most probable energy loss corrected for the density effect as described by Sternheimer[32] and experimentally verified by Hudson.[33]

Since the ionization energy loss for a relativistic electron is nearly independent of initial particle energy, the distribution function for the total energy loss by both pair members is obtained by averaging the fold of the electron and positron distributions over the converter thickness. However, in this case the fold for a given thickness is equivalent to the distribution resulting from a single particle traversing twice that thickness. This is proven in Appendix D. Therefore

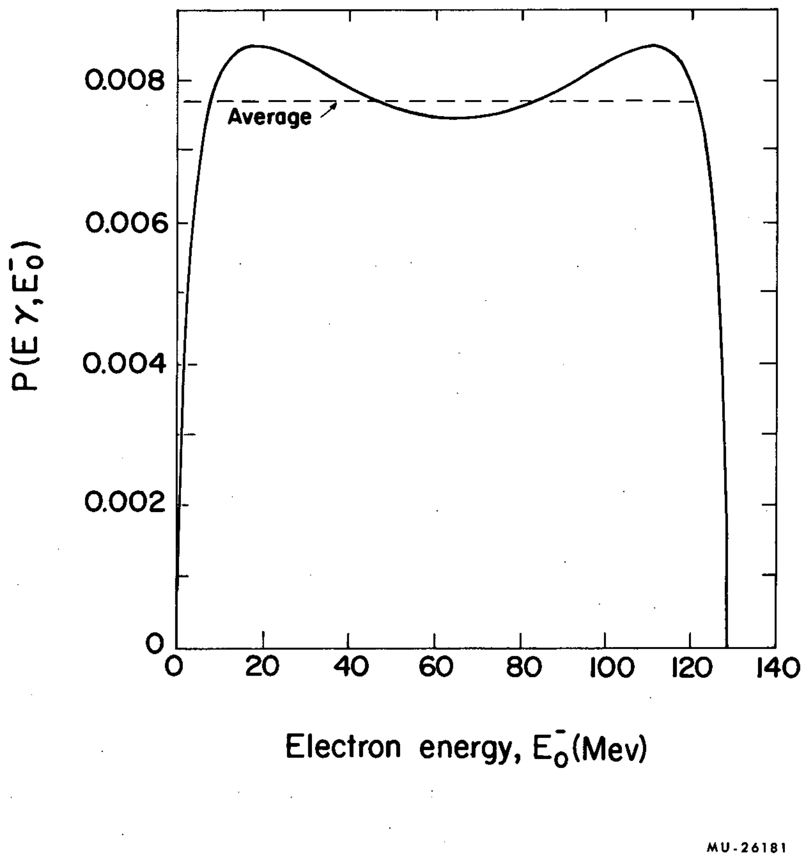

Fig. 16. Distribution of electron energies in pair production for E_γ = 129 Mev.

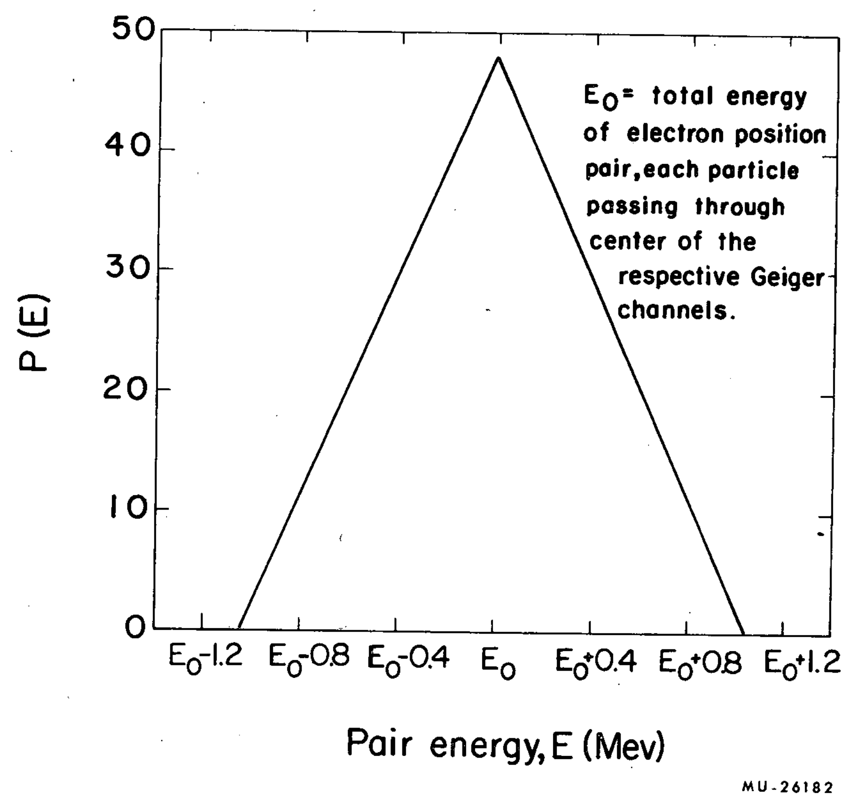

Fig. 17. Channel width resolution for B = 10, 500 gauss.

the ionization energy loss distribution for the pair was calculated by averaging the Landau distribution for an electron over twice the thickness of the actual converter. In the averaging process the tails of the Landau distribution for each converter slice were extended to an energy such that in the averaged distribution less than 1.5% of the pairs had energies lower than this.

The averaged distribution for ionization losses in converter P-3 is shown in Figure 18.

The radiation straggling distributions for electrons and positrons were computed using the sum of the cross sections for bremsstrahlung in the field of the nucleus as derived by Bethe, Davies, and Maximon[34] and in the field of the atomic electrons as given by Wheeler-Lamb.[35] To obtain the integrated radiation straggling as a function of total pair energy the individual electron and positron radiation distributions were integrated over final electron energy, converter thickness, and initial electron energy as indicated in Equation (25). The IBM 709 computer was programmed for this calculation. An explanation of the computational procedure is given in Appendix E.

The integrated radiation straggling distribution for converter P-3 and a gamma-ray energy of 129 Mev is shown in Figure 19.

Lateral Detection Efficiency

For simplicity it is assumed that there is no scattering in the converter. The lateral detection efficiency $\epsilon(E)$ is then the fraction of pairs produced with energy E which enter the detector region. For an extremely thin converter in which the electron and positron essentially lose no energy the total pair energy is equal to the incident gamma-ray energy and hence the efficiency $\epsilon(E)$ is determined entirely by the pair fragment energy distribution function $p(E_\gamma, E_0)$ and the geometry of the spectrometer. The values of this function for the range of particle energies detected by the spectrometer are quite close to the average value. Refer to Figure 16. Therefore, if a uniform distribution is assumed for $p(E_\gamma, E_0^-)$, the detection efficiency can be determined to within a few percent from the spectrometer geometry by the equations

$$\epsilon'(E) = \frac{E^+ - E_\alpha^-}{E} \quad \text{where } E = E^+ + E_\alpha^- \text{ and } E_\alpha^+ \leq E^+ \leq E_\beta^+ \tag{26}$$

and

$$\epsilon'(E) = \frac{E_\beta^+ - E^-}{E} \quad \text{where } E = E_\beta^+ + E^- \text{ and } E_\alpha^- \leq E^- \leq E_\beta^- \tag{27}$$

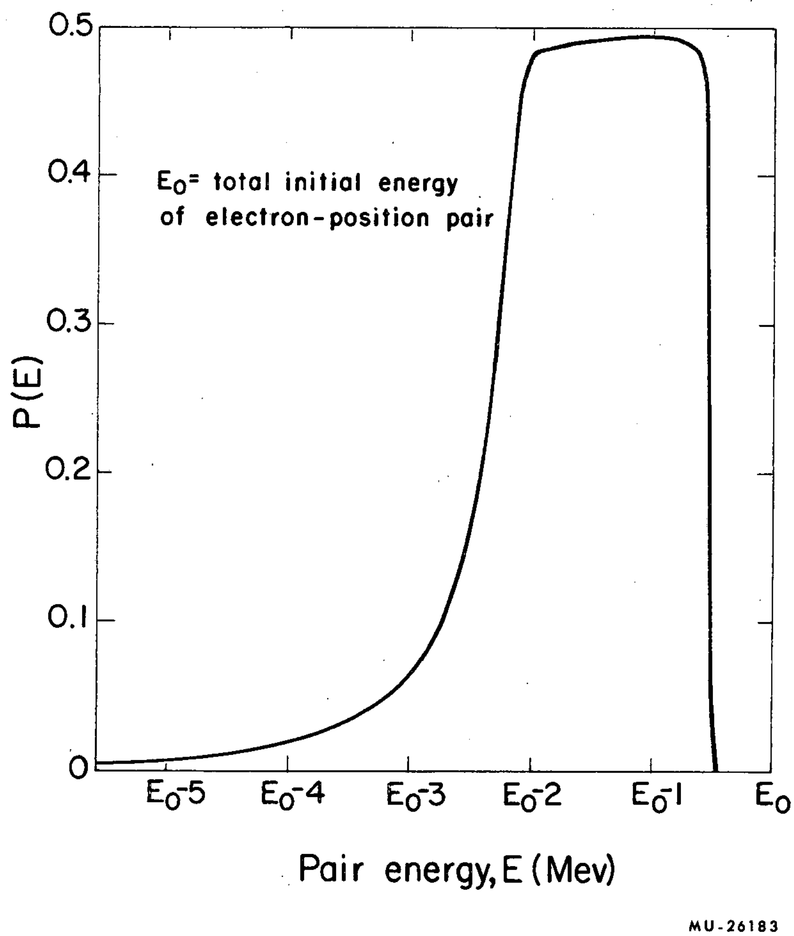

Fig. 18. Ionization energy loss distribution for converter P-3.

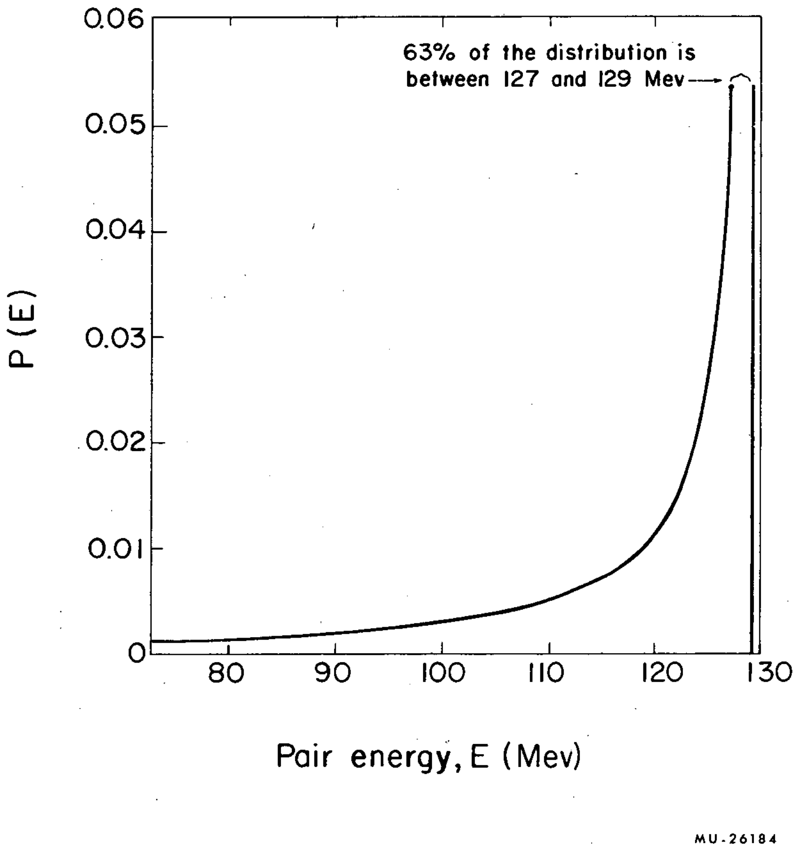

Fig. 19. Integrated radiation straggling distribution for converter P-3 and $E_\gamma = 129$ Mev.

for which E_α^-, E_β^-, E_α^+, and E_β^+ are the energies of the minimum

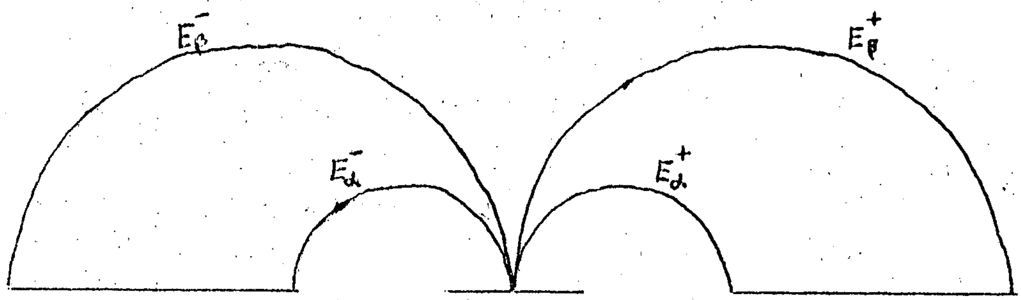

and maximum orbits originating at the converter center.

Pairs produced in a "thick" converter by gamma rays of some arbitrary fixed energy E_γ will emerge from the converter with a distribution of energies $E \leq E_\gamma$. The efficiency $\epsilon(E)$ for detecting these pairs, however, will not in general be the same as for pairs produced by gamma rays of energy E in an extremely thin converter. This is because the efficiency is determined both by the pair fragment energy distribution for the incident gamma ray and by the distribution of energy losses for the electron and positron. However for the converters used in the experiment and the gamma ray energies involved, the efficiency $\epsilon'(E)$ as determined from Equations (26) and (27) still differs by only a few percent from the correct values obtained from Equation (24). Because of this and since the correct efficiency $\epsilon(E)$ is dependent upon gamma-ray energy, $\epsilon'(E)$ was used to correct to the first approximation the measured data for the energy dependence of the detection system.

The energy dependence of the measured spectra $n_d(\Delta E)$ for a monoenergetic gamma ray should be equivalent to the calculated spectra $r(E_\gamma, E)$. Hence, if N_d is the number of pairs detected over a given energy interval and corrected for the energy dependence of the detection system with the efficiency $\epsilon'(E)$, we can write

$$N_d = \sum \frac{n_d(\Delta E)}{\epsilon'(E)} \sim \sum \frac{r(E_\gamma, E)\Delta E}{\epsilon'(E)} = \sum R'(E_\gamma, E)\Delta E. \quad (28)$$

Since the correct expression is

$$[N_d] = \sum \frac{n_d(\Delta E)}{\epsilon(E)} \sim \sum \frac{r(E_\gamma, E)\Delta E}{\epsilon(E)} = \sum R(E_\gamma, E)\Delta E \quad (29)$$

we obtain by forming the ratio of these expressions

$$\left[N_d \right] = \frac{\sum R\,(E_\gamma\,,E)\Delta E}{\sum R'(E_\gamma\,,E)\Delta E} \quad N_d \;, \tag{30}$$

which specifies the correction factor to N_d .

For the monoenergetic radiative capture gamma rays from hydrogen both functions $r(E_\gamma\,,E)$ and $R(E_\gamma\,,E)$ were calculated as a function of E using the computer program described in Appendix E and ϵ (E) was determined. The correction factor was then evaluated for the energy interval used in the analysis. For the case of the π^o gamma-ray spectrum this correction factor was calculated for several gamma-ray energies and the results averaged over the distribution.

VI. DATA AND ANALYSIS

A. Treatment of Data

In scanning the film all neon lamps which fired were recorded for each event in terms of the numbers identifying the corresponding Geiger tubes and scintillators. The total pair energy, $E = E^+ + E^-$, was then calculated according to Equation (21), which can be written as

$$E = E^+ + E^- = \frac{B}{1.313}\left(\rho^+ + \rho^-\right) = \frac{B}{5.252}\left(N^+ + N^-\right) . \qquad (31)$$

The data is presented in Tables 7, 8, 9, and 10. Table 7 indicates how all recorded events for each measurement were treated. In Tables 8, 9, and 10 the energy spectra of the acceptable events is tabulated.

The difference between the "Total gates" and "Total events recorded" columns in Table 7 is due primarily to accidental coincidences of the gate counters for which no gamma ray is involved.

For geometrical reasons a few channels in the spectrometer detection array were not used. The limits of the useful region are indicated in Figure 12 by the minimum and maximum orbits. Events in which either the electron or positron falls outside this region were rejected. The number of these is given under column A in Table 7. In addition, for each measurement the data analysis was performed over a limited range of energies (column $E_A \rightarrow E_B$) of the detected pairs. Events falling outside this range are noted in column D. Because of the relatively small variations in efficiency of the Geiger tubes (see Paragraph III-D) and since in general many different pairs of electron and positron channels correspond to the same energy, it is assumed that the Geiger tube efficiency, averaged over all constant energy channels, is independent of total pair energy. Therefore it is permissible to reject all events in which Geiger tubes on one or both sides do not fire. The number of these is given under column B. Since the efficiency of the channel scintillation counters is quite large ($>$98% for each electron or positron channel) and again since in general several sets of electron and positron channels correspond to the same energy, it is also assumed that the efficiency of the scintillation counter system is independent of total pair energy. In order to eliminate any possible energy dependent background all scintillators overlapping the Geiger tube channel which fired were also required to fire. The number of events not meeting this requirement is given in column C.

Acceptable events are classified as "good" or "extra." "Good" events are those for which either one Geiger tube or two overlapping ones fire on both electron and positron sides and for which the overlapping scintillator channel counters all fire. "Extra" events are those in which additional Geiger tubes fire and for which the scintillator and Geiger channels are in agreement.

In approximately 80% of the "extra" events less than 4 Geiger tubes fire on either side. For a large majority of these events the energy could be determined to within one or two Geiger channel widths. However, in nearly all cases the gamma-ray group involved could be determined.

Several effects contribute to cause extra Geiger tubes to fire. These include: 1) Large angle scattering in the converter causing a pair member to either intercept the 180° position at some angle or strike the pole tip or Geiger holders and scatter back into the detectors; 2) Multiple scattering in Geiger tubes or channel scintillators; 3) Accidentals; 4) Delta rays produced at the detectors and passing through near-by tubes; and 5) Back scattering from energy degrader or gate scintillation counter. Scattering calculations indicate contributions due to effect (1) are negligible. This has been confirmed by observing that the ratio of "extra" to "good" counts is independent of converter thickness T for values of T up to three times larger than the normal thickness. Since contributions from effects (2), (4), and (5) are energy dependent and due to particles traversing the detector region, it is necessary that these "extra" events be included.

The "uncertain events" in Table 7 are events in which extra Geiger tubes fired and for which either the gamma-ray group involved could not be determined or it could not be ascertained whether the incident electron or positron passed through the acceptable detector channels. If these events are equally divided among the possible alternatives, no significant influence on the ratios being measured results. Since the number of these events is small, we have chosen to ignore them.

Let a number of gamma rays, N_{γ}, be incident upon the converter. If $n_d(\Delta E)$ is the number of pairs detected in an energy channel of width ΔE, then

$$N_{\gamma} = \frac{n_d(\Delta E)}{P(E)\Delta E} , \qquad (32)$$

which by substituting Equation (23) for $P(E)\Delta E$ can be rewritten as

$$N_\gamma = \frac{n_d(\Delta E)}{\epsilon(E)} \Big/ \gamma(T)\ S(T,B) \int^{E_\gamma} I(E_\gamma) R(E_\gamma, E)\ dE_\gamma \Delta E. \qquad (33)$$

Since N_γ is independent of the energy interval over which the measurement is made, for a interval between E_A and E_B we can write

$$N_\gamma = N_d \Big/ \gamma(T)\ S(T,B) \sum_{E_A}^{E_B} \int^{E_\gamma} I(E_\gamma)\ R(E_\gamma, E)\ dE_\gamma\ \Delta E \qquad (34)$$

where

$$N_d = \sum_{E_A}^{E_B} N_d(\Delta E) = \sum_{E_A}^{E_B} \frac{n_d(\Delta E)}{\epsilon(E)}\ . \qquad (35)$$

N_d is evaluated in Tables 8, 9, and 10 for the various measurements. The measured spectra $N_d(\Delta E)$ are shown in Figures 21 and 22 for Panofsky ratio measurement I, in Figure 23 for measurement II, and in Figure 24 for the deuterium ratio measurement.

Background. The measured yields obtained for each converter with the H_2 removed from the target were approximately 0.5% as large as the corresponding yields with the H_2 in. This is consistent with the assumption that this yield is entirely due to interactions of the π^- mesons with the residual H_2 gas in the target.

The total energy range of the spectrometer over which pairs were detectable for each magnetic field setting is indicate below:

Field (Gauss)	Energy range (Mev)
5538	34.3 - 100.7
8235	51.0 - 149.7
10500	65.0 - 190.9
11013	68.2 - 200.2

It can be seen from Table 7, Column D, that for the radiative capture reaction the number of events detected with energies larger than the high energy cut off E_B is quite small. Although some of these events may be due to accidental background, the numbers are consistent with what is expected from radiative capture in flight. Since the detectable energy range above E_B is quite appreciable as can be seen above, the accidental background is assumed negligible.

B. Spectrometer Performance Checks

Several checks were made to insure that the spectrometer operation was as predicted.

With the spectrometer field set at 10,500 gauss the yeild from the radiative capture reaction in hydrogen was measured for several converter thicknesses. The "scattering in" probability $S(T,B)$ for each thickness was then determined according to Equation (34). The results are given in Figure 20. In evaluating $S(T,B)$ the calculated values for the resolution were used. However, as indicated in Paragraph VI-C the calculated spectra do not agree exactly with the measured spectra. Although the absolute corrections to $S(T,B)$ for this effect are not known, the values for the greater thicknesses should be increased somewhat. The solid curve in the figure represents the results of a scattering calculation in which it is assumed that the distribution of projected scattering angles is Gaussian. This calculation is described in Appendix B. It is noted that the calculated results in the Figure have been compared for several converter thickness with results obtained from a similar independent calculation using the exact Molière theory and agree within 1 to 2 percent.

The measured ratio of yield with converter in to yield with converter out for the Panofsky ratio runs is compared in Table 11 with that calculated using Equation (34). The calculated ratios include scattering corrections as determined from Figure 20. In addition the effective thickness of the converter counter has been taken as 0.9 the total thickness, while an equivalent thickness of 4 inches of air has been added to all converters to account for pair production in air preceding the converter. The calculated ratios are expected to be lower limits. Although the difference in the ratios for the high field is slightly greater than one standard deviation, the results are reasonable and provide good evidence that only pairs created in the converter are detected.

Since the number of gamma rays incident upon the converter, N_γ, is independent of magnetic field, a comparison of measured values of N_γ for the same gamma-ray spectra but different fields provides a check on any magnetic field effects. N_γ was determined from Equation (34) using the Panofsky ratio data for the mesic capture gamma rays at

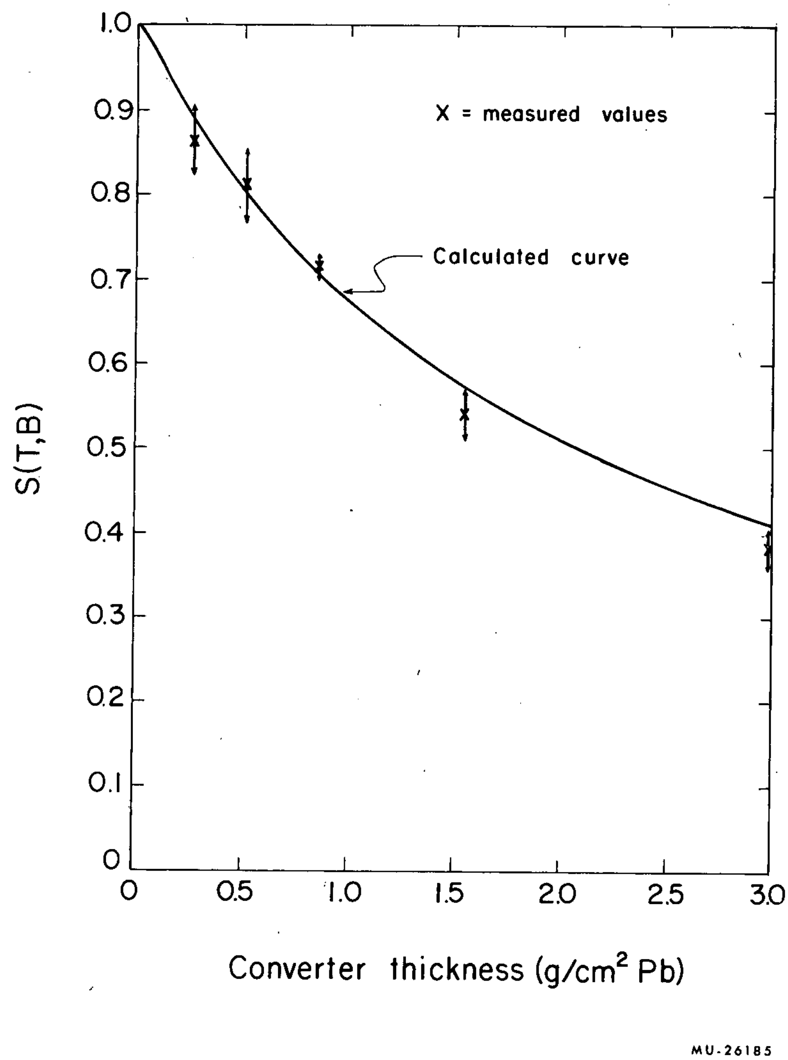

Fig. 20. "Scattering in" probability S(T, B) vs converter thickness for B = 10,500 gauss.

the low and medium fields and the radiative capture gamma rays at the medium and high fields. For this calculation an average value for the summation $\sum$ was used as described in Paragraph VI-C. The results are given in Table 12.

C. Panofsky Ratio Calculation

The measured Panofsky ratio, Formula (12), can be rewritten in terms of Equation (34) to give

$$P = (MC_1C_2C_3)\ \frac{N_{d1}}{2N_{d2}}\ \frac{\gamma_2(T)}{\gamma_1(T)}\ \frac{S_2(T,B)}{S_1(T,B)}\ \frac{\sum_2}{\sum_1} \tag{36}$$

where

$$\sum_1 = \sum_{E_{A1}}^{E_{B1}} R_1(E)\Delta E = \sum_{E_{A1}}^{E_{B1}} \int^{E_\gamma} I_1(E_\gamma) R_1(E_\gamma, E)\, dE_\gamma\, \Delta E \tag{37}$$

and

$$\sum_2 = \sum_{E_{A2}}^{E_{B2}} R_2(E_\gamma = 129 \text{ Mev}, E)\, \Delta E. \tag{38}$$

Subscripts 1 and 2 refer to the mesic capture and radiative capture gamma rays, respectively, and $I_1(E_\gamma)$ is the energy distribution frunction for the mesic capture gamma rays. The factor M normalizes the yields from the two reactions to the same numbers of π^- mesons stopping in the target. C_1, C_2, and C_3 are correction factors. C_1 compensates for the fact that the lateral detection efficiency used in evaluating N_d is not exact. This is discussed in Section V. C_2 adjusts the data for the internal conversion reactions while C_3 corrects the measured mesic capture spectrum for the contribution resulting from radiative capture gamma rays.

The values determined for the quantities in Equation (36) are given in Table 13 for the Panofsky ratio measurements I and II.

The effect produced by the converter counter has been treated by subtracting the measured yield with converter out from the yield with converter in. This can be written as

$$N_d = N_d(\text{in}) - \left(\frac{M_{in}}{M_{out}}\ \beta \right) N_d(\text{out}), \tag{39}$$

where M_{in} and M_{out} are the monitor counts for converter in and out, respectively, and the factor β compensates for the reduced number of pairs produced in the converter counter when the converter is in place. Values of N_d and M are given in Table 7.

With the pair spectrometer, electrons produced by gamma-ray Compton scattering in the converter are not detected. Considering this, the probability for pair production in the converter is given by

$$\gamma(T) = \frac{\sigma_p}{\sigma_p+\sigma_c}\left(1 - e^{-\rho(\sigma_p+\sigma_c)T}\right) \tag{40}$$

where ρ is the density and σ_p and σ_c are the cross sections for pair production and Compton scattering, respectively. The expression in the parenthesis is the total gamma-ray absorption probability while the ratio of cross sections defines the fraction of the total absorption due to pair production. The cross sections are averages over the energy spectrum considered. The sum of the cross sections for pair production in the field of the nucleus and the field of the atomic electrons was used. For the nuclear contribution the results of Bethe, Davis, and Maxamon[34] were employed with an energy dependent correction factor as discussed in NBS Circular 583. The contribution by the atomic electrons was determined from the results of Vortruba.[36] For the Compton scattering cross section the Klein-Nishina formula was used.

Although the thicknesses of the converters were selected to equalize the "scattering in" probability $S(T,B)$ for each field setting, the thickness of converter C-1 deviated slightly from the required value. To compensate for this the ratio $\frac{S_2(T,B)}{S_1(T,B)}$ for measurement I was determined from the calculated curve of $S(T,B)$ vs T for $B = 11{,}013$ gauss corresponding to that in Figure 20. $S_2(T,B)$ is obtained directly for a thickness corresponding to converter C-3 while $S_1(T,B)$ corresponds to the value given for that thickness such that the scattering is the same as for converter C-1 and $B = 5{,}538$ gauss.

The calculated spectra $R_1(E)$ and $R_2(E)$, defined in Equations (37) and (38), respectively, are shown in Figures 21 and 22 for measurement I and in Figure 23 for measurement II. The corresponding measured spectra are also given. Since the energy scales of the calculated spectra are absolute, the curves were fitted to the measured data merely by adjusting the heights. For the radiative capture gamma ray the calculated spectra was adjusted so that the areas in the peak between 124 and 130 Mev for both spectra were equal. The limits of the energy intervals over which N_d and $\sum$ have been evaluated are indicated in these figures by arrows.

It will be noted in Figures 21, 22, and 23 that the calculated spectra are consistently smaller in the tails than the measured specta.

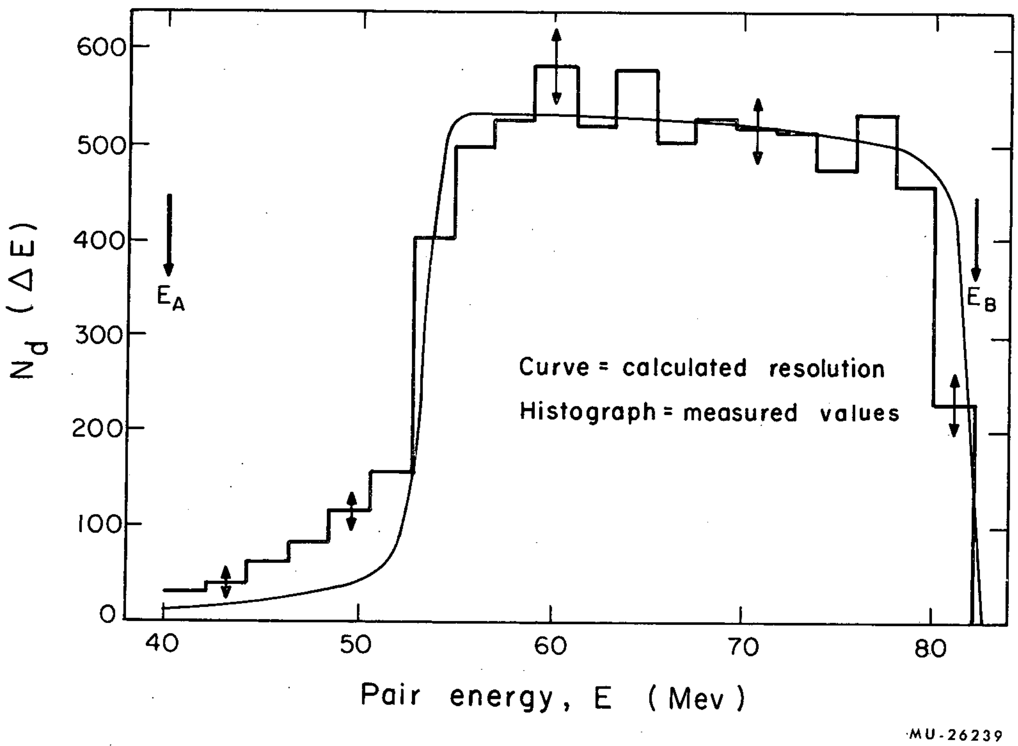

Fig. 21. Mesic capture gamma-ray spectra for B=5,538 gauss.

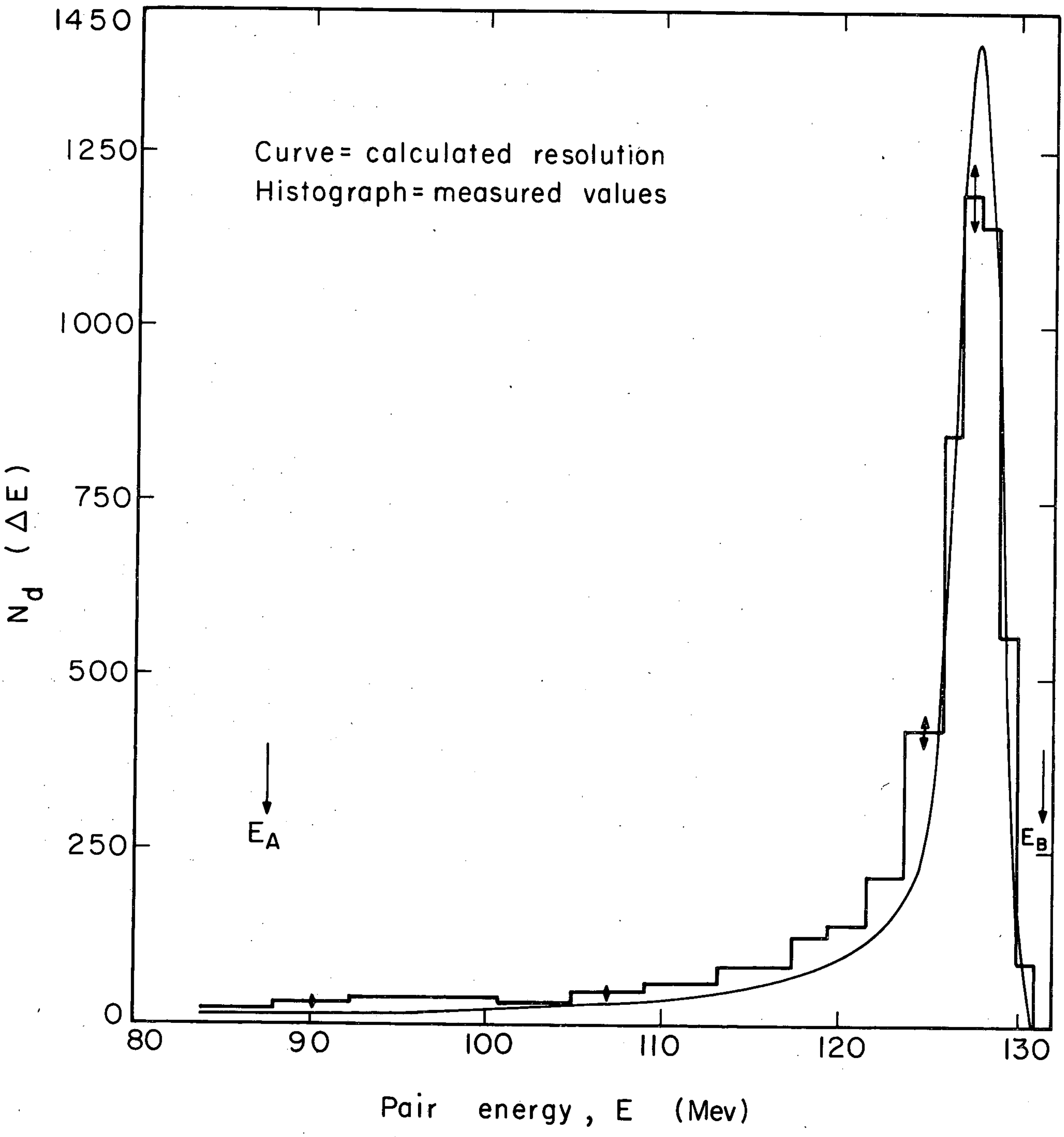

MUB-976

Fig. 22. Radiative capture gamma-ray spectra for B=11,013 gauss.

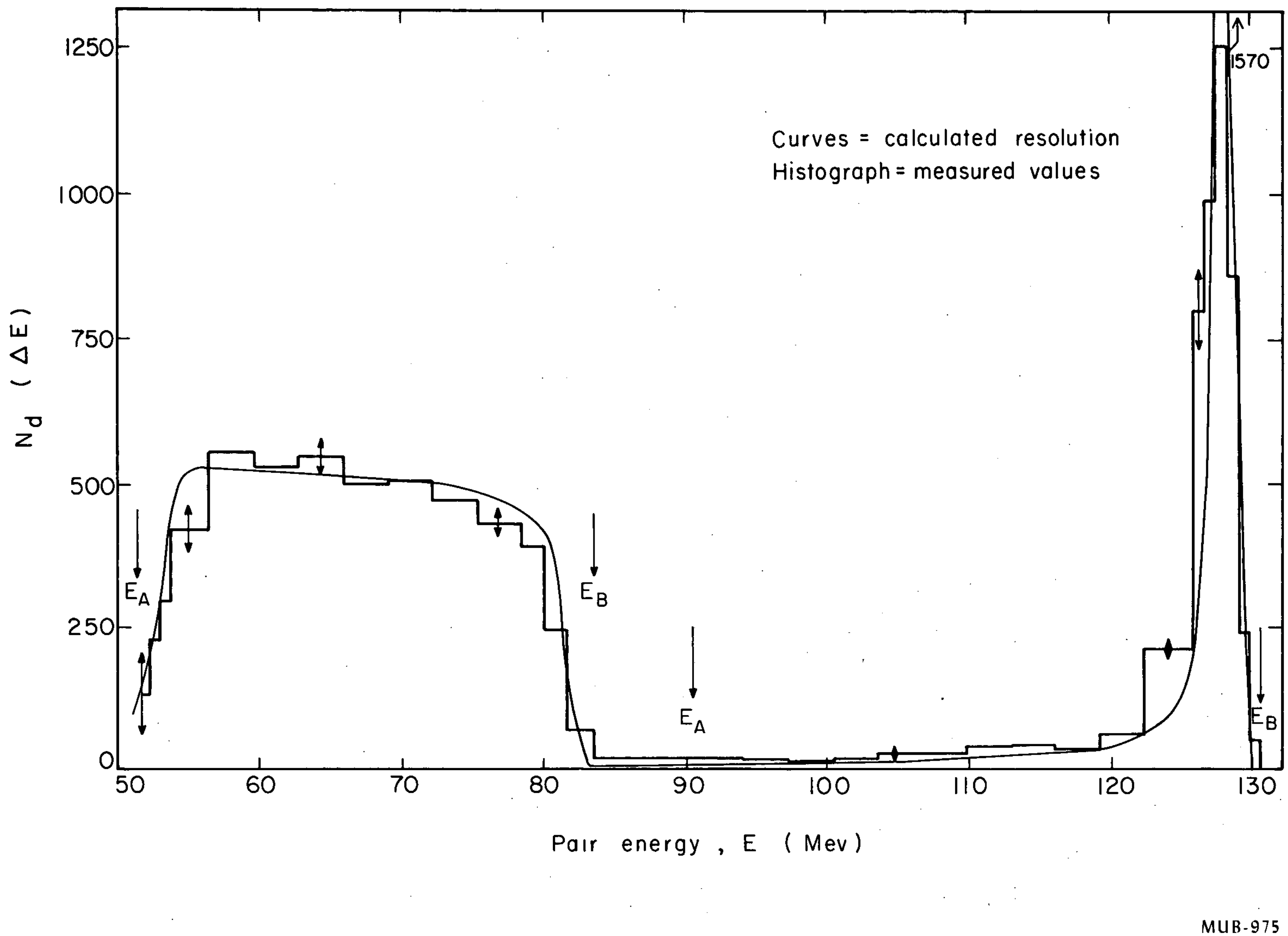

Fig. 23. Mesic capture and radiative capture gamma-ray for B = 8,235 gauss.

Possible reasons for this are discussed in Section VII. Because of this effect there is some uncertainty in determining the quantities Σ_1 and Σ_2. If it is assumed that the discrepancy between the calculated and measured spectra is due to bremsstrahlung incompletely accounted for, then, since the tail of the calculated specta is almost entirely due to bremsstrahlung, a correction to the calculated value for Σ is obtained by taking the relative discrepancy as constant from the lower cut-off energy down to zero. The value of Σ obtained in this manner is considered a lower limit. If the discrepancy is caused by other energy loss effects, such as ionization, it is believed the tail contribution would not be as great. Since the behavior in the tail is not known, the value of Σ calculated from theory is taken as the upper limit. The upper and lower limits for Σ_1, Σ_2, and the ratio $\frac{\Sigma 2}{\Sigma 1}$ derived from this analysis are tabulated below.

	MEASUREMENT I		MEASUREMENT II	
	Upper limit	Lower limit	Upper limit	Lower limit
Σ_1	.991	.978	.963	.907
Σ_2	.950	.913	.970	.948
$\frac{\Sigma 2}{\Sigma 1}$	.959	.934	1.007	1.045

It is now assumed that the correct value for the ratio $\frac{\Sigma 2}{\Sigma 1}$ lies with equal probability anywhere between the upper and lower limits. This assumption defines the values listed in Table 13.

The factor C_2 adjusts the measured data so that the results for P are expressed in terms of the definition in Equation (4).

$$P = \frac{(1a) + (1b)}{(2) + (3)} \tag{4}$$

In the present method of measurement reaction (1b) is detected only half as efficiently as (1a) while reaction (3) is never detected; due to this, C_2 is calculated to be

$$C_2 = \frac{1 + j}{(1 + j')(1 + j/2)} \tag{41}$$

where j is the branching ratio $\frac{(1b)}{(1a)}$ and j' the ratio $\frac{(3)}{(2)}$. Using the values for these ratios given in the Introduction C_2 is determined to be 0.999.

D. Deuterium Ratio S Calculation

The measured deuterium ratio, Formula (15), written in terms of Equation (34) is

$$S = \left[M(1+P) \; \frac{N_{d2}}{N_{d4}} \; \frac{\gamma_4(T)}{\gamma_2(T)} \; \frac{\sum_4}{\sum_2} \right]^{-1} \qquad (42)$$

where

$$\sum\nolimits_2 = \sum_{E_{A2}}^{E_{B2}} R_2(E_\gamma = 129 \text{ Mev}, E) \Delta E \qquad (43)$$

and

$$\sum\nolimits_4 = \sum_{E_{A4}}^{E_{B4}} R_4(E) \Delta E = \sum_{E_{A4}}^{E_{B4}} \int^{E_\gamma} I_4 (E_\gamma) R_4(E_\gamma, E) dE_\gamma \, \Delta E. \qquad (44)$$

Subscripts 2 and 4 refer to the hydrogen and deuterium radiative capture reactions, respectively, while $I_4(E_\gamma)$ is the deuterium gamma-ray energy distribution. The ratio of the term in Equation (34) envolving S(T,B) is unity and has been omitted in Equation (42). In addition, corrections to the measured spectra due to the lateral detection efficiency are nearly identical and no adjustment to S is necessary. The values determined for the quantities appearing in Equation (42) are listed in Table 14 together with the value calculated for S.

Spectrographic analysis of the deuterium used in the experiment indicated a 2.25% contamination of hydrogen. In correcting for the effects of this it is assumed that the yield due to the hydrogen is directly proportional to the concentration of hydrogen. Calculations made by Cohen, Judd, and Riddell[37] for μ^- mesic-atom systems indicate that for a $\mu^- p$ atom moving with low energy through pure deuterium the rate for transfer of the μ^- meson to a deuterium atom is $\approx 10^{10}$ sec^{-1}. However, the rate for nuclear capture of a π^- meson from a $\pi^- p$ mesic atom state is $> 25 \times 10^{10}$/sec.[18] Since it is reasonable that the probability for capture of a π^- meson into a $\pi^- p$ mesic atom state is proportional to the concentration of hydrogen and that the above transfer rate is not very different for the π^- meson, our assumption is justified. The correction was made by subtracting from the measured deuterium yield N_{d4}^{Meas} the contribution due to the hydrogen contamination and then adding that contribution which would have resulted if the hydrogen had been deuterium.

The expression for this can be written as

$$N_{d4} = N_{d4}^{Meas.} - M\,(.0225)\,N_{d2} + .0225\,N_{d4} \qquad (45)$$

which by rearranging terms becomes

$$N_{d4} = \frac{1}{1-.0225}\left(N_{d4}^{Meas.} - M(.0225)\,N_{d2}\right) \qquad (46)$$

$$= 1.0230\ \left(N_{d4}^{Meas.} - 0.0268\,N_{d2}\right)$$

$$= 1.0230 \sum \frac{n_{d4}\,(\Delta E) - 0.0268\,n_{d2}(\Delta E)}{\epsilon\,'(E)} \qquad (47)$$

N_{d4} is evaluated in Table 10.

The pair production probability for the deuterium gamma-ray distribution $\gamma_4(T)$, was calculated using for the cross section an average value weighted in terms of the gamma-ray distribution. The assumed form of the distribution was taken from the calculations of Watson and Stewart[38] for a value of the n-n scattering length as determined by Crowe and Phillips.[39]

In order to evaluate the ratio $\frac{\Sigma 4}{\Sigma 2}$, the relative contributions in the tails of the measured spectra below the low-energy cut off must be determined. The measured distributions $N_d(\Delta E)$ for both the H_2 and D_2 gamma rays are shown in Figure 24 where the distributions have been normalized to the same number of events. The cut-off energies are indicated by arrows. Since most of the contribution in the tail of the hydrogen distribution is due to radiation straggling, the contribution in the deuterium tail should be approximately 20% larger due to enhanced contributions from lower energy gamma-rays. After taking this into account the difference remaining in the two spectra at the lower cut-off energy was extrapolated linearly to zero energy. A contribution of 2.7% of the total spectra was obtained. Since the shape of actual deuterium gamma-ray spectrum is expected to fall off with decreasing energy faster than linearly, the value used for this contribution was taken as 1.4 ± 1.0. $\frac{\Sigma 4}{\Sigma 2}$ was calculated using this procedure for both the upper and lower limits of Σ_2 as determined in the manner discussed in Paragraph VI-C. The two results were averaged together to give

$$\frac{\Sigma 4}{\Sigma 2} = 0.97 \pm 0.01\ .$$

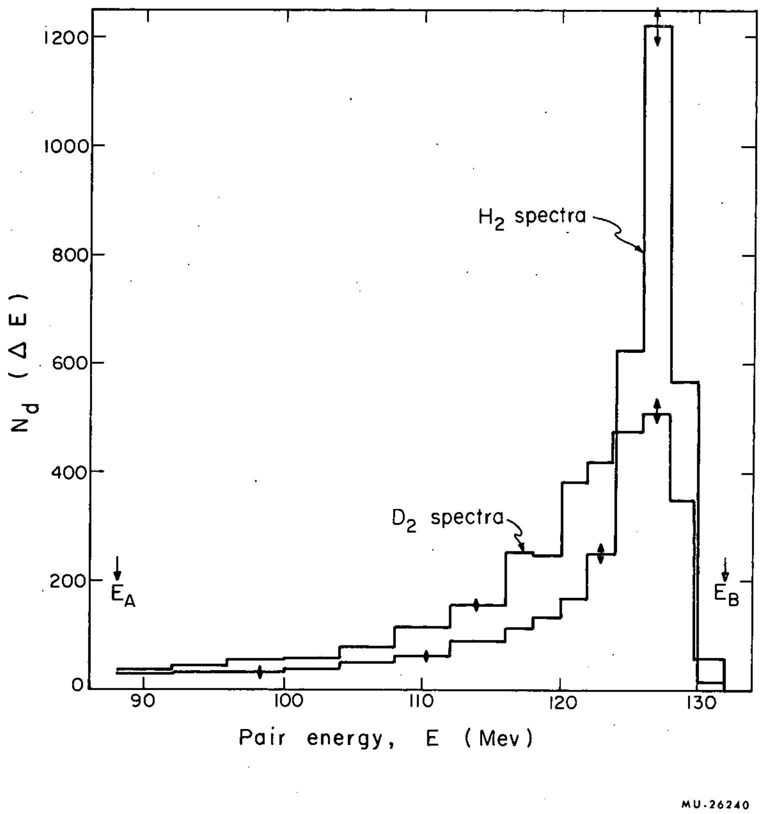

Fig. 24. Measured radiative capture gamma-ray spectra for H_2 and D_2 (B = 10,500 gauss).

In the normalization term, M, it is necessary to include in addition to the ratio of monitor counts a factor which compensates for the difference in stopping power between H_2 and D_2. The average ionization energy loss for heavy charged particles can be written

$$\frac{dE}{dx} \sim \frac{\rho Z}{Av^2} \quad f(\, v, \, \bar{I} \,) \tag{48}$$

where ρ is the mass density, Z the atomic number, A the atomic weight, v the particle velocity, and $\bar{I}$ the average ionization potential. Now Z is the same and $\bar{I}$ nearly so for both H_2 and D_2. However ρ/A for D_2 is nearly 15% larger than for H_2 and hence the stopping power 15% larger. However, since the energy spectrum of the π^- beam was not uniform, it was necessary to determine experimentally the relative number of π^- mesons stopping in the H_2 and D_2. Two independent methods were employed.

In describing the first method let t be the thickness (in gm/cm^2 of H_2 equivalent) of the energy degrader shown in Figure 25 and let r represent the range (in gm/cm^2 of H_2) of a typical π^- meson. Then the residual range of a meson upon passing through a thickness t is just r-t. Now if the function P(r) denotes the range distribution of the π^- meson beam and if q(r-t) represents the probability that a meson with residual range r-t stops in the H_2 target, we can write

$$F(t) = \int_0^\infty P(r) \; q(r-t) \; dr \tag{49}$$

where the function F(t) defines the fraction of the total beam which stops in the H_2 for a given t. This function is directly proportional to the range curve of Figure 3 with background subtracted and is shown in Figure 25. If we now assume no scattering losses for the meson beam, then all mesons with range between t and t + 1.78 gm/cm^2 will stop in the H_2 target. This specifies the function q(r-t) as equal to 1 if $0 < r - t < 1.78$ and 0 otherwise. Therefore, both functions F(t) and q(r-t) are known and the integral in Equation (49) can be unfolded to give the function P(r). P(r) is shown in Figure 26.

If the degrader thickness t is now fixed and the H_2 density increased, the target thickness in gm/cm^2 is increased and more of the meson range distribution P(r) will lie within the target. Hence by calculating F(t) for various H_2 densities the relative number of mesons stopping in the target as a function of density is obtained. The results of this are shown by the smooth curve in Figure 27. The normal density of the hydrogen and the density of deuterium corresponding to the same stopping power are indicated.

In the second method, several different values of hydrogen density were obtained by suitably pressurizing the liquid hydrogen system. See Section IV. By monitoring the reaction rate with the gamma-ray telescope the relative π^- meson stopping rate as a function of density was determined. The measured values are shown in Figure 27.

The ratio of the number of π^- mesons stopping in the D_2 target to the number stopping in the H_2 target as a result of the stopping power difference is determined from this figure as 1.13.

E. Error Analysis

The error assigned to the value for P in measurements I and II is calculated from the equation

$$\delta P = P \sqrt{\left(\frac{\delta\left(\frac{N_{d1}}{N_{d2}}\right)}{\frac{N_{d1}}{N_{d2}}}\right)^2 + \left(\frac{\delta M}{M}\right)^2 + \left(\frac{\delta\left(\frac{\gamma_2(T)}{\gamma_1(T)}\right)}{\frac{\gamma_2(T)}{\gamma_1(T)}}\right)^2 + \left(\frac{\delta\left(\frac{\Sigma_2}{\Sigma_1}\right)}{\frac{\Sigma_2}{\Sigma_1}}\right)^2} \quad . \qquad (50)$$

The standard error on the ratio of N_{d1} to N_{d2} is just

$$\delta\left(\frac{N_{d1}}{N_{d2}}\right) = \frac{N_{d1}}{N_{d2}} \sqrt{\left(\frac{\delta N_{d1}}{N_{d1}}\right)^2 + \left(\frac{\delta N_{d2}}{N_{d2}}\right)^2} \qquad (51)$$

where δN_{d1} and δN_{d2} are the standard errors on N_{d1} and N_{d2}. Since these quantities are defined by Equation (39) in which $N_d(\text{in})$ and $N_d(\text{out})$ are evaluated in accordance with Equation (35), δN_{d1} and δN_{d2} are determined by the general expression

$$\delta N_d = \sqrt{\sum\left(\frac{n_d(\Delta E)}{\epsilon'(E)^2}\right)_{\text{in}} + \left(\frac{M_{in}}{M_{out}}\,\beta\right)^2 \sum\left(\frac{n_d(\Delta E)}{\epsilon'(E)^2}\right)_{\text{out}}} \quad . \qquad (52)$$

Due to the relatively small background in the gamma-ray monitor telescope counting rate (see Figure 3), the accuracy of this monitor is limited by fluctuations in losses in the scaling system. These fluctuations were determined to be less than 2%. A comparison of the two

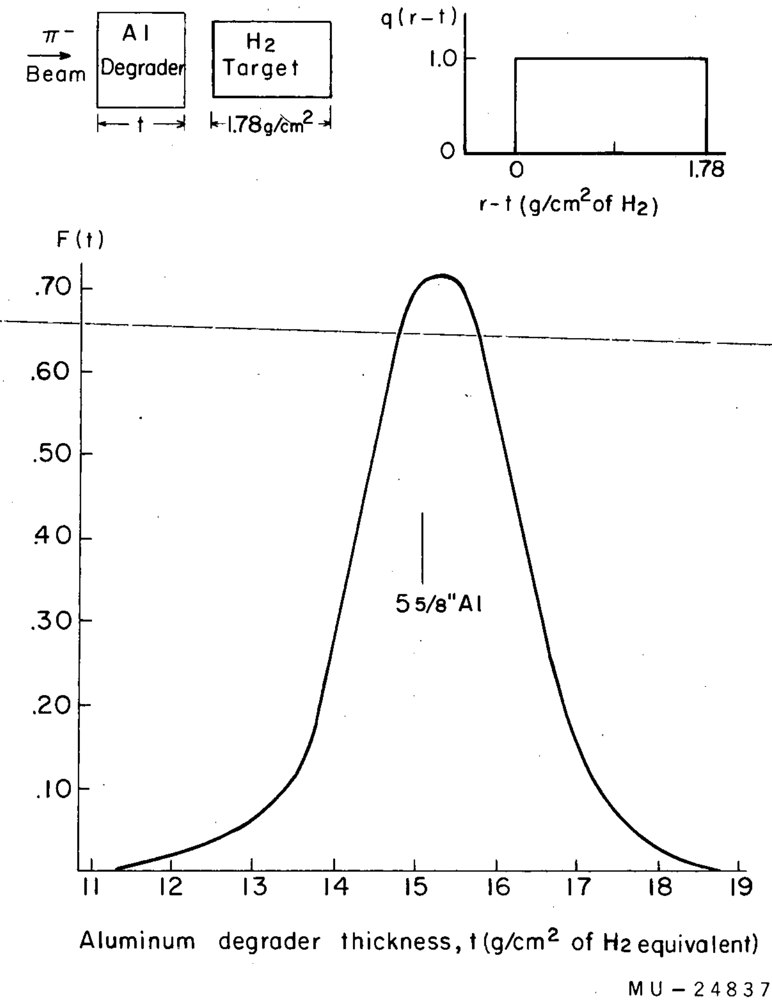

Fig. 25. Functions F(t) and q(r-t) used for range curve unfolding.

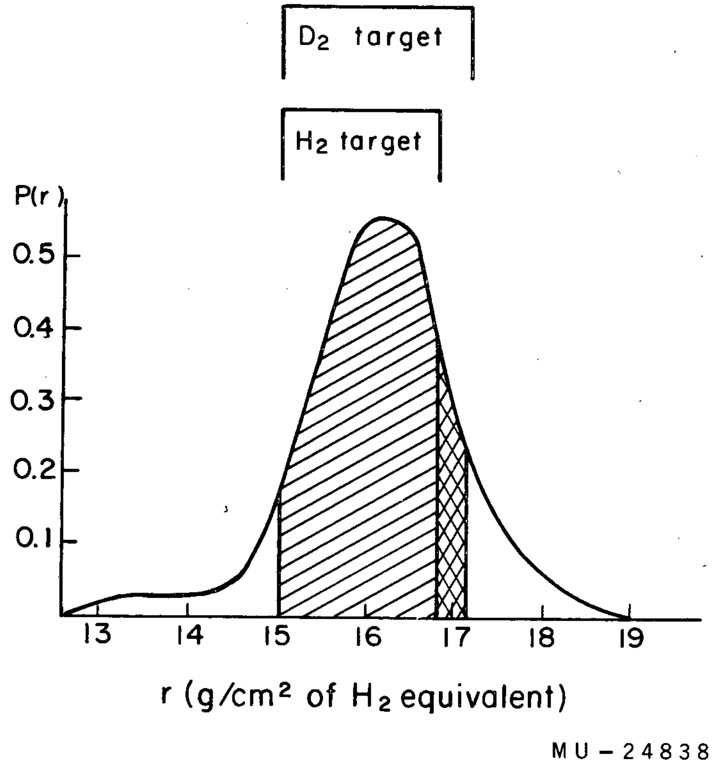

Fig. 26. Range distribution of π^- meson beam (p (r) Vs r).

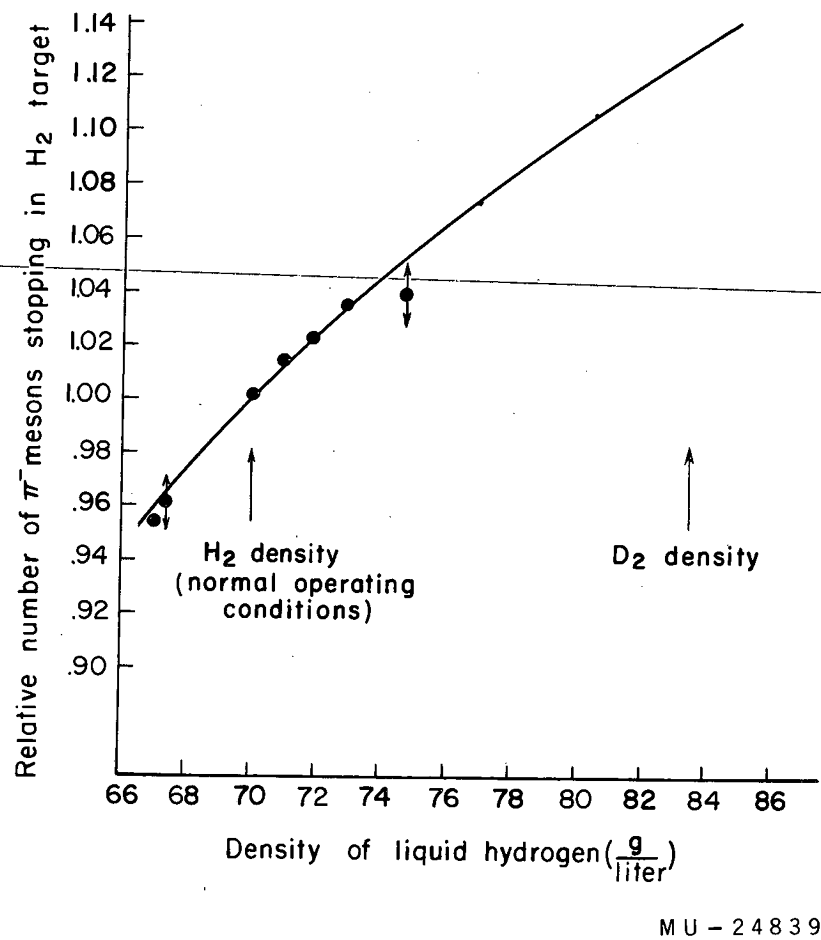

Fig. 27. Relative number of π^- mesons stopping in the hydrogen target Vs hydrogen density.

monitoring systems used showed that the average fluctuations in the relative indications were of this same magnitude. Since more than 15 runs were performed for each converter-field situation and the various types of runs alternated, we estimate the monitoring error to be 0.3%.

The ratio of the pair production probabilities can be approximated by

$$\frac{\gamma_2(T)}{\gamma_1(T)} \sim \frac{1 - e^{-\rho\sigma_2 T_2}}{1 - e^{-\rho\sigma_1 T_1}} \approx \frac{\rho\sigma_2 T_2}{\rho\sigma_1 T_1} \tag{53}$$

since the probabilities are small compared to one. Therefore, the fractional error on the ratio of probabilities is just the fractional error on the ratio of cross sections

$$\delta\left(\frac{\gamma_2(T)}{\gamma_1(T)}\right) \Big/ \frac{\gamma_2(T)}{\gamma_1(T)} = \delta\left(\frac{\sigma_2}{\sigma_1}\right) \Big/ \frac{\sigma_2}{\sigma_1} \,. \tag{54}$$

The errors in σ_1 and σ_2 arise from the approximation made in the calculations of Bethe, Davis, and Maximon.[34] Since the ratio only is involved here, the error should be small. We estimate a 1% error in the ratio.

The error assigned to the deuterium ratio S is determined from the expression

$$\delta S = S\sqrt{\left(\frac{\delta\left(\frac{N_{d2}}{N_{d4}}\right)}{\frac{N_{d2}}{N_{d4}}}\right)^2 + \left(\frac{\delta(1+P)}{1+P}\right)^2 + \left(\frac{\delta M}{M}\right)^2 + \left(\frac{\delta\left(\frac{\Sigma_4}{\Sigma_2}\right)}{\frac{\Sigma_4}{\Sigma_2}}\right)^2} \,. \tag{55}$$

The expression for the standard error on the ratio of N_{d2} to N_{d4} has the same form as Equation (51). However, δN_{d2} and δN_{d4} are evaluated in this case by the general expression

$$\delta N_d = \sqrt{\sum\left(\frac{n_d(\Delta E)}{\epsilon'(E)^2}\right)} \,. \tag{56}$$

In addition to a 0.3% error on the ratio of monitor counts as described previously, a 1% error has been assigned to the ratio of the numbers of π^- mesons stopping in H_2 and D_2 due to the difference in stopping power. This error arises from the uncertainty in the range curve unfolding.

VII. RESULTS AND DISCUSSION

The final results for the Panofsky ratio and the deuterium ratio S are:

$$P = 1.51 \pm 0.04$$

$$S = 3.16 \pm 0.10 \quad .$$

Here P is the weighted average of the values determined for measurements I and II in Paragraph VI-C.

Previous measurements of P are shown in Table 1. If each of these is weighted according to the quoted error, the value obtained is

$$P = 1.54 \pm 0.02.$$

Our result is in complete agreement.

The value of S obtained here is significantly higher than the results of previous measurements, which are shown in Table 2. It is also considerably higher than that calculated from Equation 11. (See Table 3). Although the reason for this disagreement is not known, systematic errors on this measurement are believed to be quite small since the same converter and the same magnetic field are used for both the hydrogen and deuterium runs and since both radiative capture gamma-ray spectra are quite similar.

As was indicated in Paragraph VI-C a discrepancy exists between the shape of the theoretical spectra and the measured spectra. The values determined for P and S depend upon the assumed cause of this discrepancy. In obtaining the above results we have assumed that the discrepancy is caused by energy losses of the electrons and positrons in the converter incompletely accounted for . In the following paragraphs we discuss the various causes of this effect which have been considered, and the probable magnitude of their contribution. These include: 1) Reduced energy gamma rays entering the spectrometer; 2) apparent or real energy loss effects associated with the spectrometer design; and 3) uncertainties in the energy loss of high energy relativistic electrons.

The first possible cause might involve either nuclear reaction in which lower energy gamma rays are produced or gamma rays with reduced energy produced by Compton effect or shower formation on the collimator walls. It is noted that the measured hydrogen radiative capture spectrum can be reconstructed very well with a combination of 82% of the theoretical hydrogen spectra plus 18% of the measured deuterium spectra. Since the hydrogen used had the normal isotopic abundance, then, if this apparent agreement were meaningful, it would imply a very high transfer rate of the π^- meson between hydrogen and deuterium. However, as indicated in Paragraph VI-D the transfer rate even in pure deuterium is believed to be relatively small. This, together with the fact that the π^0 gamma-ray spectra also displays the same effect, leads us to consider this explanation as quite improbable. Rough calculations of Compton scattering of gamma rays in the collimator walls indicate the contribution of reduced energy gamma rays due to this should be much smaller than the observed effect. It seems unlikely that this process or shower formation would yield a gamma-ray spectrum required to explain the discrepancy. However, if Compton scattering on the collimator walls were assumed to be the cause, from a comparison of the measured and theoretical spectra it is estimated that the quoted value for P would be reduced by 6% and S would remain essentially unchanged. This reduced value for P, however, would disagree significantly with previous measured values of P.

With respect to the second possible cause, an electron undergoing a large angle scattering in the converter may enter the detector region with apparent lower energy. For an apparent energy decrease of a few Mev it is very probable that several Geiger tubes would be triggered and the event classified as "extra," as defined in Paragraph VI-A. However, the measured spectra is essentially the same whether these events are included or not. The scattering calculations also indicate that these large angle scattering events are too rare to explain the observed effect. They also indicate that the number of electrons scattered off the pole tip or the Geiger holders and back into the detector region simulating a reduced energy electron is much too small to account for the observed results.

There are two processes by which the electron and positron can lose energy in the converter, bremsstrahlung and ionization. The bremsstrahlung cross section employed (see paragraph VI-C) is believed to be accurate to within a few percent, but has not been experimentally verified. A summary of previous bremsstrahlung measurements is given in the review article by Koch and Motz.[40] With respect to ionization, the Landow ionization energy loss distribution for high energy electrons has been checked by Hudson[33] who obtains slight deviations in the shape of the distribution near the high energy end and excellent agreement with respect to the most probable energy loss. However, very little experimental information is available with regard to the tail of the distribution.

VIII. ACKNOWLEDGEMENTS

I would like to thank Professor Kenneth M. Crowe for suggesting this problem and for his valuable guidance and assistance.

Among the many persons who contributed to this experiment I would like to thank especially the following for help during the experiment and from whom many valuable suggestions were offered: Bart Czirr, Hans Kruger, Bob Beck, Tin Maung, Phil Beilin, Gordon Bingham, Bob Shafer, John Whitsel and George Sheldon.

Many hours of steady beam were supplied by the cyclotron crew under the direction of J. Vale and L. Houser.

To Marianne White for typing the manuscript I wish to express my thanks.

I would like to especially thank my wife, Ellen, for her patience and understanding during my graduate career.

Work done under the auspices of the U. S. Atomic Energy Commission.

IX. APPENDICIES

A. Derivation of S and P

If it is assumed that the transition rate for nuclear capture from a bound state mesic atom is proportional to the square of the pion wave function at the position of the proton, then we can write

$$\omega_b(\pi^- + p \rightarrow \pi^\circ + n) = v\ |\phi_H(0)|^2 \sigma(\pi^- + p \rightarrow \pi^\circ + n) \qquad (57)$$

where the relative velocity v and cross section σ correspond to the in-flight process and $\phi_H(0)$ is the wave function for the mesic atom state from which capture occurs evaluated at the position of the proton. If charge independence in the pion nucleon interaction is assumed, the charge exchange cross section can be expressed as

$$\sigma(\pi^- + p \rightarrow \pi^\circ + n) = \frac{8\pi}{9} \frac{1}{q^2} (a_3 - a_1)^2 , \qquad (58)$$

where a_3 and a_1 are the S-wave scattering lengths for isotopic spin states 3/2 and 1/2, respectively, and q is the incident c.m. pion momentum. A first order correction due to the $\pi^- - \pi^\circ$ mass difference changes Equation (58) to

$$\sigma(\pi^- + p \rightarrow \pi^\circ + n) = \frac{8\pi}{9} \frac{1}{q^2} \frac{v_o}{v_-} (a_3 - a_1)^2 \qquad (59)$$

where v_o and v_- are the c.m. velocities of the π° and π^- mesons w.r.t. the nucleons. Substituting Equation (59) into (57) yields

$$\omega_b(\pi^- + p \rightarrow \pi^\circ + n) = \frac{8\pi}{9} \frac{v_o v}{q^2 v_-} |\phi_H(0)|^2 (a_3 - a_1)^2 \qquad (60)$$

In analogy to Equation (57) the bound state radiative capture reaction rate is

$$\omega_b(\pi^- + p \rightarrow \gamma + n) = v\ |\phi_H(0)|^2 \sigma(\pi^- + p \rightarrow \gamma + n) . \qquad (61)$$

Using detailed balancing the in-flight cross section can be expressed as

$$\sigma(\pi^- + p \rightarrow \gamma + n) = \frac{2k^2}{q^2}\sigma(\gamma + n \rightarrow \pi^- + p) \tag{62}$$

where k is the incident photon c.m. momentum. If R is defined as

$$R = \frac{\sigma(\gamma + n \rightarrow \pi^- + p)}{\sigma(\gamma + p \rightarrow \pi^+ + n)} \tag{63}$$

then Equation (62) may be rewritten as

$$\sigma(\pi^- + p \rightarrow \gamma + n) = \frac{2k^2}{q^2} R\sigma(\gamma + p \rightarrow \pi^+ + n) \quad . \tag{64}$$

Substituting Equation (64) into (61) yields

$$\omega_b(\pi^- + p \rightarrow \gamma + n) = \frac{2k^2 v}{q^2} R \left|\phi_H(0)\right|^2 \sigma(\gamma + p \rightarrow \pi^+ + n). \tag{65}$$

By forming the ratio of Equations (60) and (65) we obtain for the Panofsky ratio,

$$P = \frac{4\pi}{9R} \frac{v_o}{v\,k^2} \frac{(a_3 - a_1)^2}{\sigma(\gamma + p \rightarrow \pi^+ + n)} \quad . \tag{66}$$

Since at threshold for the photoproduction reaction

$$k = \frac{1 + \frac{\mu}{2M}}{1 + \frac{\mu}{M}} , \tag{67}$$

and we have

$$v = q \tag{68}$$

where μ and M are the pion and nucleon rest masses, Equation (66) can be rewritten in the final form as

$$P = \frac{4\pi}{9R} \frac{v_o}{q} \frac{(1+\frac{\mu}{M})^2}{(1+\frac{\mu}{2M})^2} \frac{(a_3 - a_1)^2}{\sigma(\gamma + p \rightarrow \pi^+ + n)} \quad . \tag{69}$$

In analogy wit Equation (57)

$$\omega_b(\pi^- + d \rightarrow 2n) = v^D \,|\phi_D(0)|^2\, \sigma(\pi^- + d \rightarrow 2n) \; . \tag{70}$$

The in-flight cross section can be expressed using detailed balancing as

$$\sigma(\pi^- + d \rightarrow 2n) = \frac{2}{3}\, \frac{P_n^2}{q^{D2}}\, \sigma(n + n \rightarrow \pi^- + d) \tag{71}$$

where P_n is the c.m. neutron momentum and q^D the c.m. pion momentum in the π^- - d system. Now by charge symmetry

$$\sigma(n + n \rightarrow \pi^- + d) = \sigma(p + p \rightarrow \pi^+ + d) \tag{72}$$

and hence by substituting Equations (71) and (72) into Equation (70), we obtain

$$\omega_b(\pi^- + d \rightarrow 2n) = \frac{2}{3}\, v^D\, |\phi_D(0)|^2\, \frac{P_n^2}{q^{D2}}\, \sigma(p + p \rightarrow \pi^+ + d). \tag{73}$$

If the ratio T is defined according to

$$\omega_b(\pi^- + d \rightarrow \gamma + 2n) = T\, \omega_b(\pi^- + p \rightarrow \gamma + n) \tag{74}$$

and Equation (61) substituted into (74), we can write

$$\omega_b\,(\pi^- + d \rightarrow \gamma + 2n) = T\, v\, |\phi_H(0)|^2\, \sigma\,(\pi^- + p \rightarrow \gamma + n) \; . \tag{75}$$

Using Equation (64), Equation (75) can be expressed as

$$\omega_b(\pi^- + d \rightarrow \gamma + 2n) = \frac{2\pi k^2 v}{q^2}\, |\phi_H(0)|^2\, R\, \sigma(\gamma + p \rightarrow \pi^+ + n). \tag{76}$$

By forming the ratio of Equations (73) and (76) the following expression for S is obtained

$$S = \frac{1}{3TR} \quad \frac{v^D}{v} \quad \frac{q^2}{q^{D2}} \quad \frac{|\phi_D(0)|^2}{|\phi_H(0)|^2} \quad \frac{P_n^2}{k^2} \quad \frac{\sigma(p+p\rightarrow\pi^+ + d)}{\sigma(\gamma + p\rightarrow\pi^+ + n)} \, . \qquad (77)$$

By the relations

$$T = T' \frac{|\phi_D(0)|^2}{|\phi_H(0)|^2}$$

$$P_n^2 \approx M \text{ at threshold}$$

$$v = q(1 + \frac{\mu}{M}) \text{ and}$$

$$v^D = q^D(1 + \frac{\mu}{2M}) \, .$$

S can be expressed in the final form,

$$S = \frac{M}{3T'R} \quad \frac{q}{q^D} \, \frac{1 + \frac{\mu}{M}}{1 + \frac{\mu}{2M}} \quad \frac{\sigma(p + p\rightarrow\pi^+ + d)}{\sigma(\gamma + p\rightarrow\pi^+ + n)} \, . \qquad (78)$$

B. Calculation of S(T,B)

The projected angle α is defined as that angle which the projection of the momentum vector (for an electron or positron leaving the converter) on a vertical plane perpendicular to the converter makes with the converter normal. Angles for which the momentum vector is directed below the horizontal are considered negative.

The multiple scattering distribution for projected angles as derived by Moliere can be written as

$$f(\alpha)d\alpha = \frac{1}{\sqrt{\pi}\;\theta_1\sqrt{\beta}} \left[e^{-\frac{\alpha^2}{\theta_1^2\beta}} + \frac{f_1(\alpha)}{\beta} + \dots \right] d\alpha \qquad (79)$$

The first term is Gaussian and normalized to one. The remaining terms are much smaller and can be considered as corrections to the Gaussian term. The variable θ_1 in Equation (79) is defined according to

$$\theta_1^2 = 0.157 \; \frac{Z(Z+1)}{A} \; \frac{t}{E^2} \quad (t \text{ in } \frac{gm}{cm^2}, \; E \text{ in Mev})$$

and β can be determined to better than 1% from the formula

$$\beta = 21.81 + 2.37\, q - 0.02\, q^2$$

where

$$q = \ln_{10}\left[Z^{-2/3}\ \frac{t}{A}\ \frac{Z^2}{2.12 \times 10^4 + 3.76\, Z^2} \right].$$

Since a Gaussian approximation for multiple scattering is known to hold quite well for angles less than 2 or 3 times the rms width if the width is appropriately chosen, and because the Molière distribution predicts quite accurately the scattering, the Gaussian term in Equation (79) with rms width $\alpha' = \frac{\theta_1\sqrt{\beta}}{\sqrt{2}}$ is used in this calculation and is rewritten below:

$$f(\alpha)d\alpha = \frac{1}{\sqrt{\pi}\,\theta_1\sqrt{\beta}}\ e^{-\alpha^2/\theta_1^2\beta}\, d\alpha = \frac{1}{\sqrt{2\pi}\,\alpha'}\ e^{-\alpha^2/2\alpha'^2}\, d\alpha. \qquad (80)$$

The "scattering in" probability S(T,B) is defined in Appendix C, Equation (92) as

$$S(T,B) = \frac{1}{\gamma(T)} \sum_{t=0}^{T} \gamma(t,T)\ S(t,B)\,\Delta t \qquad (81)$$

where S(t,B) is given as

$$S(t,B) = \int^{z} Z(z) \int_{h_a}^{h_b} P_h(t,z,B,h)dh \int_{h_a}^{h_b} P_{h'}(t,z,B,h')dh'dz. \qquad (82)$$

These functions are all defined in Appendix C. Since $P_h(t,z,B,h)$ is the distribution function for vertical heights of the electrons at the detector, it can be written as

$$P_h(t,z,B,h)dh = \int^{\text{all }\alpha} f(t,E^-,\alpha)\ g(\alpha,z,\rho,h)d\alpha\, dh \qquad (83)$$

where $f(t,E^-,\alpha)$ is the distribution function in projected angle for an electron of energy E^- traversing a thickness t of material and $g(\alpha,z,\rho,h)dh$ is the probability that an electron originating in the converter at the vertical position z, having angle α and radius of curvature ρ, will strike the detector with height between h and dh.

For small scattering angles an electron with α and ρ will travel a distance $\pi\rho$ from converter to the 180° orbit position as indicated in the diagram below.

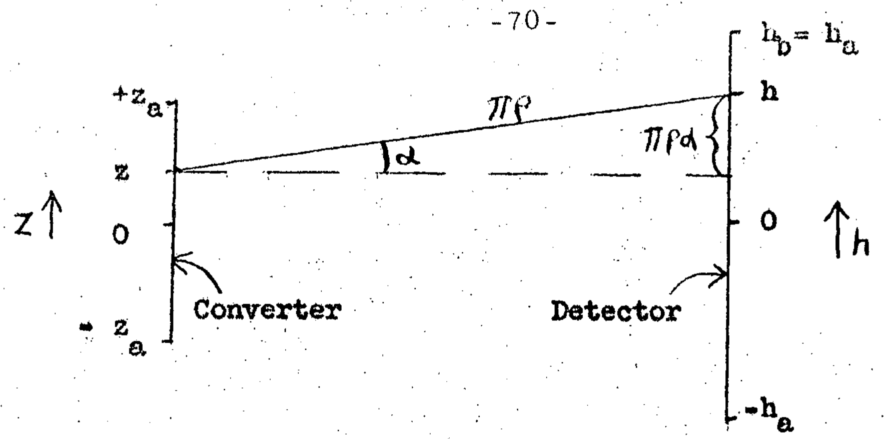

Here the actual circular orbits are represented as straight lines. The converter height is $2z_a$ and the detector height is $2h_a$. If the vertical position of the electron at the converter is z, then the vertical height h at the detector is just

$$h = \pi\rho\alpha + z . \tag{84}$$

This specifies the function $g(\alpha, z, \rho, h)$ as the Kronecker delta function

$$g(\alpha, z, \rho, h) = \frac{1}{\pi\rho}\delta\left(\alpha - \frac{h-z}{\pi\rho}\right) . \tag{85}$$

Substituting Equation (85) into (83) we obtain

$$P_h(t,z,B,h)dh = \frac{1}{\pi\rho}\int^{\text{all }\alpha} f(t,E^-,\alpha)\,\delta\left(\alpha - \frac{h-z}{\pi\rho}\right)d\alpha\;\; dh = \frac{1}{\pi\rho}f\left(t,E^-,\frac{h-z}{\pi\rho}\right)dh. \tag{86}$$

It has been shown in Paragraph III-D of the text that this distribution is independent of electron energy. Therefore the electron and positron distribution functions P_h and $P_{h'}$ in Equation (82) are identical. Substituting Equation (86) back into Equation (82) and using Equation (80), we obtain

$$S(t,B) = \int_{-z_a}^{+z_a} Z(z) \left[\int_{-h_a}^{+h_a} \frac{1}{\pi\rho\sqrt{2\pi}\alpha'}\, e^{-\frac{(h-z)^2}{2(\pi\rho\alpha')^2}}\, dh \right]^2 \tag{87}$$

Since gamma-rays are incident uniformly over the converter, the function $Z(z)$ is just $\frac{1}{2z_a}$; and if we let $y = \frac{h-z}{\sqrt{2}\pi\rho\alpha'}$, Equation (87) can be rewritten as

$$S(t,B) = \frac{1}{2\pi z_a}\int_{-z_a}^{+z_a} \left[\int_{-h_a-z/\sqrt{2}\pi\rho\alpha'}^{h_a-z/\sqrt{2}\pi\rho\alpha'} e^{-y^2}\, dy \right]^2 dz .$$

This equation was numerically integrated using the IBM 650 computer to obtain $S(t,B)$ as a function of t for the different magnetic fields used. The "scattering in" probability $S(T,B)$ was then calculated from Equation (81).

C. Spectrometer Detection Probability Calculation

Let $P(E)dE$ be the probability that a gamma ray selected at random from a spectrum with energy distribution $I(E_\gamma)$ will pair produce in the converter and the resulting pairs be detected with total energy between E and $E+dE$.

$$P(E)dE = \int^{E_\gamma}\int^{y}\int^{z}\int^{t}\int^{E_o^-}\int^{E_1^-} I(E_\gamma)Y(y)\,Z(z)\,\gamma(E_\gamma,t,T)\,P(E_\gamma,E_o^-) \times F^-(E_\gamma,t,E_o^-,E_1^-)\,F^+(E_\gamma-E_o^-,t,E-E_1^-) \quad (88)$$

$$\times\, G(E_o^-,E_\gamma-E_o^-,E_1^-,E-E_1^-,t,y,z,B)\,dE_1^-\,dE_o^-\,dt\,dz\,dy\,dE_\gamma\,dE$$

where

$$G = \int_{h_a}^{h_b} P_h(E_o^-,E_1^-,t,z,B,h)\,dh\; H^-(E_1^-,y,B,r_a<r<r_b) \quad (89)$$

$$\times \int_{h_a}^{h_b} P_{h'}(E_o^- - E_\gamma,E-E_1^-,t,z,B,h')\,dh'\; H^+(E-E_1^-,y,B,r_a<r'<r_b).$$

Here E_γ is the gamma-ray energy, y the lateral converter position, z the vertical converter position, t the thickness of converter from the position of pair creation to the exit face, T the total converter thickness, E_o^- the initial electron energy, E_1^- the final electron energy after traversing the converter, h and h' the respective vertical heights at the detector for electron and positron, r and r' the respective lateral positions at the detector for electron and positron, and B the magnetic field. The functions are defined at the end of this Appendix.

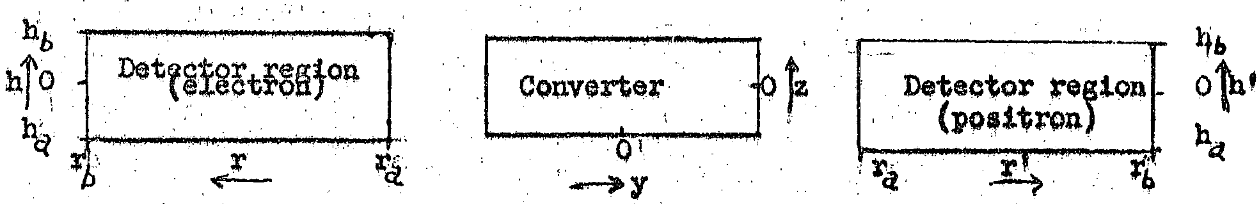

The distribution functions for vertical height at the detector, P_h and $P_{h'}$ are derived in Appendix B and it is noted that for the geometry used these functions are independent of the particle energies.

Substituting Equation (89) into (88) we obtain

$$
\begin{aligned}
P(E)dE = & \int^{E_\gamma} I(E_\gamma) \int^{y} Y(y) \int^{E_o^-} P(E_\gamma, E_o^-) \int^{t} \gamma(E_\gamma, t, T) \\
& \times \int^{E_1^-} F^-(E_\gamma, t, E_o^-, E_1^-)\, H^-(E_1^-, y, B, r_a < r < r_b) F^+(E_\gamma - E_o^-, t, E-E_1^-) \\
& \times H^+(E-E_1^-, y, B, r_a < r' < r_b) dE_1^-\, dE_o^-\, dy\, dE_\gamma \qquad (90) \\
& \times \underline{\int^{z} Z(z) \int_{h_a}^{h_b} P_h(t,z,B,h)dh \int_{h_a}^{h_b} P_{h'}(t,z,B,h')dh'dz}\; dtdE.
\end{aligned}
$$

The underlined integral above is the probability that for a given t and B the vertical height for both electron and positron at the 180° orbit position is between ha and hb. Let us call this the "scatter-ing-in" probability and refer to it as $S(t,B)$. Also let $\frac{\text{Ave. over } E_\gamma}{\gamma(E_\gamma, t, T)} = \gamma(t,T)$, then we may rewrite (90) to give

$$
\begin{aligned}
P(E)dE = & \sum_{t=0}^{T} \gamma(t,T)S(t,B)dt \int^{E_\gamma} I(E_\gamma) \int^{y} Y(y) \int^{E_o^-} P(E_\gamma, E_o^-) \\
& \times \int^{t} \frac{\gamma(E_\gamma, t, T)S(t,B)}{\sum_{t=0}^{T} \gamma(t,T)S(t,B)dt} \int^{E_1^-} F^-(E_\gamma, t, E_o^-, E_1^-) H^-(E_1^-, y, B, r_a < r < r_b) \\
& \times F^+(E_\gamma - E_o^-, t, E-E_1^-)\, H^+(E-E_1^-, y, B, r_a < r' < r_b) dE_1^-\, dt \\
& \times dE_o^-\, dy\, dE_\gamma\, dE\,. \qquad (91)
\end{aligned}
$$

Now if $S(T,B)$ is the probability for "scattering in" averaged over the converter thickness, we can write

$$
S(T,B) = \frac{\sum_{t=0}^{T} \gamma(t,T)\, S(t,B)\, \Delta t}{\gamma(T)} \qquad (92)
$$

where

$$
\gamma(T) = \sum_{t=0}^{T} \gamma(t,T)\, \Delta t \qquad (93)
$$

is the total probability for pair production in the converter of thickness T averaged over the energy spectrum considered. We define the weighting function $W(E_\gamma, t, B)$ as

$$W(E_\gamma, t, B) = \frac{\gamma(E_\gamma, t, T)S(t, B)}{\sum_{t=0}^{T} \gamma(t, T)S(t, B)\Delta t} = \frac{\gamma(E_\gamma, t, T)\, S(t, B)}{\gamma(T)\, S(T, B)} \quad . \quad (94)$$

Equation (91) can now be expressed as

$$P(E)dE = \gamma(T)S(T,B) \int^{E_\gamma} I(E_\gamma) \int^{y} Y(y) \int^{E_o^-} P(E_\gamma, E_o^-)$$
$$\times \int^{t} W(E_\gamma, t, B) \int^{E_1^-} F^-(E_\gamma, t, E_o^-, E_1^-) H^-(E_1^-, y, B, r_a < r < r_b)$$
$$\times F^+(E_\gamma - E_o^-, t, E-E_1^-)\, H^+(E-E_1^-, y, B, r_a < r' < r_b) dE_1^-$$
$$\times dt dE_o^- dy dE_\gamma \; dE \; . \qquad (95)$$

If we define a resolution function $r(E_\gamma, E)$ as

$$r(E_\gamma, E) = \int^{y} Y(y) \int^{E_o^-} P(E_\gamma, E_o^-) \int^{t} W(E_\gamma, t, B) \int^{E_1^-} F^- H^- F^+ H^+$$
$$\times \; dE_1^- \, dt \, dE_o^- \, dy \quad , \qquad (96)$$

Equation (95) can be rewritten as

$$P(E)dE = \gamma(T)\, S(T, B) \int^{E_\gamma} I(E_\gamma) r(E_\gamma, E)\, dE_\gamma \; dE \; . \qquad (97)$$

The functions H^- and H^+ occurring in $r(E_\gamma, E)$ effectively serve to cut off the respective functions F^- and F^+ at certain values of the energies E_1^- and $E-E_1^-$ corresponding to the detector lateral limits. If $\epsilon(E)$ is called the lateral detection efficiency defined as the efficiency for both members of a pair of energy E to intercept the 180° position within the lateral detector limits, Equation (97) can be rewritten as

$$P(E)dE = \gamma(T)S(T,B) \int^{E_\gamma} I(E_\gamma) R(E_\gamma, E) dE_\gamma \; \epsilon(E) dE, \qquad (98)$$

where

$$R(E_\gamma ,E)=\int^{E_o^-} P(E_\gamma ,E_o^-) \int^{t} W(E_\gamma ,t,B) \int^{E_1^-} F^-(E_\gamma ,T,E_o^-,E_1^-)$$

$$\times F^+(E_\gamma -E_o^-,t,E-E_1^-)\, dE_1^- \, dt \, dE_o^- . \qquad (99)$$

This function $R(E_\gamma ,E)$ is termed the energy adjusted resolution function.

Definition of functions in Appendix C

$I(E_\gamma)dE_\gamma$ — Probability that a gamma ray has energy between E_γ and $E_\gamma + dE_\gamma$.

$Y(y)dY$ — Probability that a gamma ray is incident on the converter with lateral position between y and y + dy.

$Z(z)dz$ — Probability that a gamma ray is incident on the converter with vertical position between z and z + dz.

$\gamma(E_\gamma, t, T)dt$ — Probability that a gamma ray of energy E_γ incident on a converter of thickness T will pair produce in a thickness interval between t and t + dt.

$\gamma(T)$ — Total probability for pair production in a thickness T averaged over the incident gamma-ray spectrum.

$P(E_\gamma, E_o^-)dE_o^-$ — Probability that in pair production by a gamma ray of energy E_γ the electron produced has an energy between E_o^- and $E_o^- + dE_o^-$.

$F^-(E_\gamma, t, E_o^-, E_1^-)dE_1^-$

Probability that an electron of initial energy E_o^- produced by a gamma ray of energy E_γ will have a final energy between E_1^- and $E_1^- \pm dE_1^-$ after passing through a thickness t of material.

$F^+(E_\gamma - E_o^-, t, E - E_1^-)$

Probability that a positron of initial energy $E_\gamma - E_o^-$ produced in pair production by a gamma ray with E_γ will have a final energy between $E - E_1^-$ and $E - E_1^- + dE_1^-$ after passing through a thickness t of material.

$P_h(E_o^-, E_1^-, t, z, B, h)dh$

Probability that an electron of initial energy E_o^- having converter vertical coordinate z and final energy E_1^- after passing through a thickness t of the converter will intercept the 180 degree orbit position with vertical height between h and dh.

$H^-(E_1^-, y, B, r_a < r < r_b)$

This function is equal to 1 if $r_a < (2.626 \frac{E_1^-}{B} + y) < r_b$ and 0 otherwise.

D. Proof of Ionization Energy Loss Theorem

It is assumed that the ionization energy loss distribution for an electron or positron is independent of initial particle energy. Let p(t,k) represent this distribution where p(t,k)dk is defined as the probability that either particle passing through a thickness t of material loses an energy between k and k + dk. If both particles go through a thickness t, the distribution function representing the total energy loss by both particles can be written in terms of the folding integral

$$F(t,K)=\int^{k} P(t,k)\; P(t,\; K-k)dk \tag{100}$$

where F(t,K)dK is the probability for a total energy loss between K and K + dK. We wish to show that the distribution F(t,K) is identical to that for a single electron going through a thickness 2t of the same material.

The ionization energy loss distribution for a particle after passing half way through a converter of total thickness 2t is just P(t,k). Since this function defines the distribution of energies entering the second half of the converter, we can write for the final energy loss distribution F(t,K')

$$F(t,K') = \int^{k} P(t,k)\; f(t,k,K')dk \quad , \tag{101}$$

where f(t,k,K')dK' is the probability that an electron which has lost an energy k in the first half will have an additional energy loss between K'-k and K'-k + dK' in the second half. However, since the energy loss is assumed independent of initial energy

$$f(t,k,K')dK' = P(t,K'-k)dK'$$

and hence Equation (101) can be rewritten as

$$F(t,K') = \int^{k} P(t,k)\; P(t,K'-k)dk. \tag{102}$$

The distributions in Equations (100) and (102) are identical. Q.E.D.

E. Description of Radiation Straggling Calculation

If bremsstrahlung energy losses alone are considered, the energy distribution $p(E_\gamma, E)$ of the pairs produced by a beam of gamma rays of energy E_γ incident upon the converter can be written as

$$P(E_\gamma, E) = \int^{E_o^-} P(E_\gamma, E_o^-) \int_0^T W(E_\gamma, t, B) \int^{E_1^-} F^+ (E_\gamma - E_o^-, t, E-E_1^-) \times F^-(E_o^-, t, E_1^-) \; dE_1^- \, dt \, dE_o^- \quad . \tag{103}$$

This is identical in form with Equation (25) in the text; however, in Equation (103) the functions F^- and F^+ pertain only to radiation straggling. It is noted that for a given t and initial electron and positron energies the integral over E_1^- $\left[\text{i.e. the function } F(E_o^-, E_\gamma - E_o^-, t, E) \right]$ is the "folding" integral. Hence, $P(E_\gamma, E)$ is obtained by averaging this fold over the converter thickness and initial electron energy.

The converter of thickness T was divided into

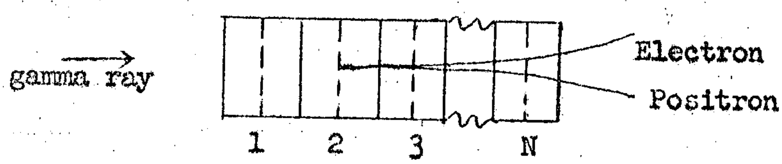

N slices as indicated above. For both electrons and positrons originating at the center of a slice with energy E_o^- and $E_\gamma - E_o^-$, respectively, and traversing the residual thickness of converter the radiation straggling distribution was calculated. These two distributions were then folded together with respect to the final electron energy E_1^-. This process was repeated for all N slices and the resulting distribution averaged together with the weighting function $W(E_\gamma, t, B)$. This procedure was repeated for a large number of values of E_o^-. Numerical integration over E_o^- for many values of E gave the distribution $P(E_\gamma, E)$.

The radiation straggling distribution function $F^-(E_o^-, \Delta t, E_1^-)$ resulting from an electron of initial energy E_o^- traversing a sufficiently thin slice Δt can be written in terms of the bremsstrahlung (differential in energy) cross section $\sigma_{E_1^-}(E_o^-, E_1^-)$ as

$$F^-(E_o^-, \Delta t, E_1^-) dE_1^- = N_a \sigma_{E_1^-}(E_o^-, E_1^-) \Delta t \; dE_1^-$$

where N_a is the number of atoms per unit volume. For bremsstrahlung in the field of the nucleus the differential cross section as given by Davies, Bethe, and Maximon[34] is

$$\sigma_{E_1^-}(E_o^-, E_1^-) = \frac{4Z^2 r_o^2}{137(E_o^- - E_1^-)} \left\{ \left(1 + \left(\frac{E_1^-}{E_o^-}\right)^2 \right) \times \left[\frac{\phi_1(\gamma)}{4} - \frac{1}{3} \ln Z - f(Z) \right] - \left(\frac{2}{3} \frac{E_1^-}{E_o^-} \right) \times \left[\frac{\phi_2(\gamma)}{4} - \frac{1}{3} \ln Z - f(Z) \right] \right\} \quad (104)$$

where $F(Z)$ is a Coulomb correction term and $\phi_1(\gamma)$ and $\phi_2(\gamma)$ are functions given by Wheeler and Lamb.[35] The cross section used for electron-electron bremsstrahlung is similar in form to Equation (104); however, Z^2 is replaced by Z and slightly different functions are used in place of $\phi_1(\gamma)$ and $\phi_2(\gamma)$. In determining the straggling distribution for an electron originating at the center of a slice and traversing the residual thickness, Δt was taken equal to a half slice thickness. The distribution resulting from passing through the first slice was then used as the input energy spectrum to the second half slice. In this half slice the energy distributions were calculated for all input energies and the contributions to each final energy summed using the input distribution as the weighting function. This procedure was carried out for all half slices in the residual thickness.

The thickness of the slice Δt was determined in the following manner. For particular initial energies of the electron and positron the integral of the fold with respect to the converter thickness was evaluated for several values of slice thickness. The value of the distribution function obtained for a given energy E was then plotted against slice thickness. From the asymptotic nature of the curve the slice thickness required for any desired accuracy of the distribution function could be determined. For the converter thicknesses employed here $N = 7$ slices proved adequate.

X. Definition of Symbols

A	Atomic weight.
B	Magnetic field intensity.
c	Velocity of light.
e	Charge of electron.
E	Total electron-positron pair energy.
E_A	Low energy cut off used in analysis of measured and calculated spectra.
E_B	High energy cut off used in analysis of measured and calculated spectra.
E^-	Electron energy.
E_o^-	Electron energy immediately after pair production.
E_1^-	Electron energy at exit face of converter.
E^+	Positron energy.
E_γ	Gamma ray energy.
h	Vertical height of particle at the 180 degree orbit position.
$\bar{I}$	Average ionization potential.
M	Normalization factor.
M	Nucleon rest mass.
N_γ	Number of gamma rays incident on the converter; $N_{1\gamma}$ = number from mesic capture reaction, $N_{2\gamma}$ = number from radiative capture reaction in H_2. $N_{4\gamma}$ = number from radiative capture reaction in D_2.
$n_d(\Delta E)$	Number of pairs detected within the Geiger channel energy interval ΔE; $n_{d1}(\Delta E)$ = number from the mesic capture reaction, $n_{d2}(\Delta E)$ = number from the radiative capture reaction in H_2, $n_{d4}(\Delta E)$ = number from the radiative capture reaction in D_2.
N_d	Number of pairs detected in the energy interval $E_A \Rightarrow E_B$ corrected for the lateral detection efficiency; N_{d1} = number from the mesic capture reaction, N_{d2} = number from the radiative capture reaction in H_2, N_{d4} = number from the radiative capture reaction in D_2,

	N_d(in) = number with converter in,
	N_d(out) = number with converter out.
N^-	Geiger tube location number (electron side).
N^+	Geiger tube location number (positron side).
P	Particle momentum.
r	Range of π^- meson (in gm/cm^2 of H_2).
T	Total converter thickness.
t	Distance from position of pair creation in converter to exit face.
t	Meson beam degrader thickness (gm/cm^2 of H_2 equiv.).
v	Velocity.
Z	Atomic number.
α'	Root mean square projected scattering angle.
ρ	Radius of curvature.
ρ^-	Electron radius of curvature.
ρ^+	Positron radius of curvature.
μ	Pion rest mass.
σ_p	Pair production cross section.
σ_c	Compton scattering cross section.

XI. TABLES

Table I. Measurements of the Panofsky Ratio

Experimenter	Reference	Method	Panofsky ratio
Panofsky et al.	2	Pair Spectrometer	0.94 ± 0.30
Sargent et al.	3	Cloud Chamber	1.10 ± 0.50
Cassels, et al.	4	Total absorption Cerenkov detector	1.50 ± 0.15
Fischer et al.	5	Total absorption Cerenkov detector	1.87 ± 0.10
Kuehner et al.	6	Pair Spectrometer	1.60 ± 0.17
Koller	7	Total absorption Cerenkov detector	1.46 ± 0.10
Derrick et al.	8	Bubble Chamber	1.47 ± 0.10
Samios	9	Bubble Chamber	1.62 ± 0.06
Jones, et al.	10	Total absorption Cerenkov detector	1.56 ± 0.05
Cocconi et al.	11	Total absorption NaI detector	1.533 ± 0.021
This Experiment		Pair Spectrometer	1.51 ± 0.04

Table 2. Measurements of the Deuterium Ratios (S and R)

Experiment	Reference	Method	S	R
Panofsky et al.	2	Pair Spectrometer	2.36 ± 0.74	-0.003 ±0.073
Chinowsky and Steinberger	12	Counter detection of both reactions	1.5 ± 0.8	
Chinowsky and Steinberger	13			-.0034 ±0.0043
Kuehner et al.	14	Pair Spectrometer	2.36 ±0.36	
This Experiment		Pair Spectrometer	3.16 ±0.10	

Table 3. **Comparison of measured and calculated values for P and S**

	Calculated Value	Measured Value
P	1.55 ± 0.24	1.53 ± 0.02
S	1.70 ± 0.36	3.16 ± 0.10

Calculated values based upon	Ref.
$a_3 - a_1 = (0.245 \pm 0.007)q$	25
$\sigma(\gamma + p \to \pi^+ + n) = (0.19 \pm 0.02)q \times 10^{-27}\ cm^2$	27
$\sigma(p + p \to \pi^+ + d) = (1.38 \pm 0.15)q^D \times 10^{-28} cm^2$	28
$R = 1.33 \pm 0.14$	25
$T = 0.77 \pm 0.08$	26

Measured values based upon

P - weighted average of all experiments

S - this experiment

Table 4. Converter characteristics and applications

Converter Nomenclature	Thickness gm/cm^2 Pb	Thickness gm/cm^2 Lucite Backing (CH)	Applications
C-1	.2293	.152	Panofsky ratio
C-2	.4781	.152	Panofsky ratio
C-3	.8102	.152	Panofsky ratio and Deuterium ratio
C-4	1.527	.152	Spectrometer checks
C-5	2.938	.152	Spectrometer checks

Table 5. Scintillation counter characteristics

Plastic Scintillation Counter	Dimensions (inches) Thickness	Length	Height	Notes
1	0.050	6	4	
2N	0.500	17.5	5	Scintillator and lucite tapered lengthwise
3P	0.500	17.5	5	Scintillator and lucite tapered lengthwise
4N	0.125	16	5	2-in. lengths of scintillator and lucite alternated
5N	0.125	12	5	4-in. lengths of scintillator and lucite alternated
6N	0.125	8	5	
7P	0.125	16	5	2-in. lengths of scintillator and lucite alternated
8P	0.125	12	5	4-in. lengths of scintillator and lucite alternated
9P	0.125	8	5	

Table 6. Converter-field combinations used in cyclotron runs

Measurement	Converter	Mag. Field	H_2 or D_2
Panofsky ratio I	C-1	5538	H_2
Panofsky ratio II	C-2	8235	H_2
Panofsky ratio I	C-3	11,013	H_2
Panofsky ratio I	out	5538	H_2
Panofsky ratio II	out	8235	H_2
Panofsky ratio I	out	11,013	H_2
Deuterium ratio	C-3	10,500	H_2
Deuterium ratio	C-3	10,500	D_2
Yield vs. Thickness	C-1	10,500	H_2
Yield vs. Thickness	C-2	10,500	H_2
Yield vs. Thickness	C-4	10,500	H_2
Yield vs. Thickness	C-5	10,500	H_2

Table 7. Treatment of measured data

Measure-ment	Field	Conver-ter	H_2 or D_2	Relative Monitor cts	Total Gates	Total Events Recorded	Events rejects A	B	C	D	Uncertain Events	Energy Interval $E_A \rightarrow E_B$	Acceptable events Good	Extra	Total (n_d)	N_d
anofsky atio I	5538	C-1	H_2	39.43	4954	4851	378	1458	210	11(high) 6(low)	11	40.1-82.2	2214	563	2777	7358
anofsky atio I	5538	out	H_2	16.83	278	251	21	93	11	2(low)	2	40.1-82.2	92	30	122	324
anofsky ratio I	11013	C-3	H_2	36.85	7051	6922	1437	1685	219	564(low) 8(high)	21	87.5-131.5	2475	513	2988	7057
Panofsky ratio I	11013	out	H_2	15.63	190	164	34	56	3	13(low)		87.5-131.5	51	7	58	130
Panofsky ratio II	8235	C-2	H_2	56.31	11376	11196	1682	3847	362	60(between) 4(high)	31	51.4-83.5 90.5-130.5	3445 959	503 283	3948 1242	17929 6385
Panofsky ratio II	8235	out	H_2	30.33	485	440	57	192	17	2(between)	3	51.4-83.5 90.5-130.5	106 27	24 12	130 39	573 210
Deuterium ratio S	10500	C-3	H_2	992.8	8517	8401	1673	1931	347	1062(low) 6(high)	14	88-132	2787	580	3367	7542
Deuterium ratio S	10500	C-3	D_2	1057.2	3916	3831	380	822	201	77(low) 4(high)	8	88-132	1987	352	2339	5320

Table 8. Data (Panofsky ratio I spectrum)

B = 5538 gauss					
		Converter C-1		Converter out	
ΔE(Mev)	$\epsilon' E$	$n_d(\Delta E)$	$\frac{n_d(\Delta E)}{\epsilon'(E)}$	$n_d(\Delta E)$	$\frac{n_d(\Delta E)}{\epsilon'(E)}$
40.1-42.2	.1664	5	30.0		
42.2-44.3	.207	8	38.6	1	4.8
-46.4	.244	15	61.4		
-48.5	.278	23	82.7	1	3.6
-50.6	.309	36	116.5	1	3.2
-52.7	.337	53	157.2	4	11.9
-54.8	.363	146	402.2	5	13.8
-56.9	.387	193	498.7	7	18.1
-59.0	.394	208	527.9	10	25.4
-61.2	.412	241	584.9	13	31.5
-63.3	.432	225	520.8	10	23.1
-65.4	.450	261	580.0	12	26.7
-67.5	.468	235	502.1	12	25.6
-69.6	.454	240	528.6	4	8.8
-71.7	.410	212	517.0	12	29.3
-73.8	.370	190	513.5	10	27.0
-75.9	.331	157	474.3	6	18.1
-78.0	.295	158	535.5	7	23.7
-80.1	.260	119	457.6	3	11.5
-82.2	.227	52	229.1	4	17.6
		2777	7358 = N_d(in)	122	324 = N_d(out)

Table 8. Data (Panofsky ratio I spectrum) Continued

B = 11,013 gauss					
		Converter C-3		Converter Out	
ΔE(Mev)	$\epsilon'(E)$	$n_d(\Delta E)$	$\frac{n_d(\Delta E)}{\epsilon'(E)}$	$n_d(\Delta E)$	$\frac{n_d(\Delta E)}{\epsilon'(E)}$
87.5-88.1	.224	3	13.4		
88.1-92.3	.244	32	131.1		
-96.5	.278	44	158.3		
-100.7	.309	51	165.0	1	3.2
-104.8	.337	46	136.5	1	3.0
-109.0	.363	71	195.6		
-113.2	.387	96	248.1		
-117.4	.394	135	342.6	1	2.5
-119.5	.407	104	255.5		
-121.6	.417	120	287.7	1	2.4
-123.7	.427	184	430.9	2	4.7
-125.8	.437	371	848.9		
-126.8	.444	376	846.8	3	6.8
-127.9	.448	533	1189.7	10	22.3
-128.9	.453	519	1145.6	17	37.5
-130.0	.457	256	560.1	15	32.8
-131.0	.462	43	93.1	7	15.2
-131.5	.465	4	8.6		
		2988	7057.5 = N_d(in)	58	130.5 = N_d(out)

Table 9. Data (Panofsky ratio II spectrum)

ΔE(Mev)	$\epsilon'(E)$	Converter C-2 $n_d(\Delta E)$	Converter C-2 $\frac{n_d(\Delta E)}{\epsilon'(E)}$	Converter out $n_d(\Delta E)$	Converter out $\frac{n_d(\Delta E)}{\epsilon'(E)}$
51.4-52.1	.0153	2	130.7	1	65.4
52.1-52.9	.0299	7	234.1		
-53.7	.0442	13	294.1		
-56.4	.0750	122	1626.6	3	40.0
-59.6	.1213	270	2225.9	3	24.7
-62.7	.1664	354	2127.4	9	54.1
-65.9	.2070	455	2198.1	11	53.1
-69.0	.244	486	1991.8	14	57.4
-72.1	.278	562	2021.6	18	64.7
-75.3	.307	582	1895.8	22	71.7
-78.4	.332	583	1756.0	25	75.3
-80.0	.352	277	786.9	9	25.6
-81.5	.364	181	497.3	11	30.2
-83.5	.377	54	143.2	4	10.6
		3948	17929.5 = N_d(in)	130	572.8 = N_d(out)

Table 9. Data (Panofsky ratio II spectrum) Continued

		Converter C-2		Converter out	
ΔE(Mev)	$\epsilon'(E)$	$n_d(\Delta E)$	$\frac{n_d(\Delta E)}{\epsilon'(E)}$	$n_d(\Delta E)$	$\frac{n_d(\Delta E)}{\epsilon'(E)}$
90.5-94.1	.427	34	79.6	1	2.3
-97.2	.447	27	60.4		
-100.3	.461	24	52.1	2	4.3
-103.5	.446	32	71.7		
-106.6	.403	44	109.2	2	5.0
-109.8	.362	41	113.3	3	8.3
-112.9	.324	51	157.4	1	3.1
-116.0	.288	48	166.7	1	3.5
-119.2	.253	36	142.3	1	4.0
-122.3	.221	58	262.4		
-125.8	.1902	170	893.7	4	21.0
-126.6	.1707	139	814.2		
-127.4	.1636	165	1008.5	3	18.3
-128.2	.1564	200	1278.7	7	44.8
-129.0	.1493	131	877.4	10	67.0
-129.7	.1424	35	245.8	4	28.1
-130.5	.1355	7	51.7		
		1242	6385.1 = N_d(in)	39	209.7 = N_d(out)

Table 10. Data (Deuterium ratio S spectrum)

		H_2 in Target		D_2 in Target			
ΔE(Mev)	$\epsilon'(E)$	$n_{d2}(\Delta E)$	$\frac{n_{d2}(\Delta E)}{\epsilon'(E)}$	$n_{d4}(\Delta E)$	$\frac{n_{d4}(\Delta E)}{\epsilon'(E)}$	0.0268 $\times n_{d2}(\Delta E)$	$\frac{0.0268\, n_{d2}(\Delta E)}{\epsilon'(E)}$
88-92	.278	33	118.7	26	93.5	1	3.6
92-96	.309	40	129.4	39	126.2	1	3.2
96-100	.337	45	133.5	52	154.3	1	3.0
100-104	.363	56	154.3	59	162.5	2	5.5
104-108	.387	80	206.7	85	219.6	2	5.2
108-112	.394	98	248.7	127	322.3	3	7.6
112-116	.412	145	351.9	180	436.9	4	9.7
116-118	.427	97	227.2	152	356.0	3	7.0
118-120	.437	117	267.7	153	350.1	3	6.9
120-122	.446	151	338.6	239	535.9	4	9.0
122-124	.455	228	501.1	269	591.2	6	13.2
124-126	.464	580	1250.0	320	689.6	15	32.3
126-128	.472	1154	2444.9	363	769.1	31	65.7
128-130	.465	528	1135.5	239	514.0	14	30.1
130-132	.443	15	33.9	36	81.3		
		3367	7542.1 = N_{d2}	2339	5402.5 = N_{d4}Meas.	90	202.0 = 0.0268 N_{d2}

$$N_{d4} = 1.023(N_{d4}\text{Meas} - 0.0268\, N_{d2})$$

$$= 5320$$

Table 11. Converter in-converter out ratios

Magnetic Field (gauss)	Reaction involved	Conv.	Converter in-out Ratios	
			Calculated	Measured
5538	$\pi^- + p \rightarrow \pi^0 + n$	C-1	8.86	8.70 ± 0.80
8235	$\pi^- + p \rightarrow \pi^0 + n$	C-2	16.97	18.33 ± 1.70
8235	$\pi^- + p \rightarrow \gamma + n$	C-2	16.97	15.92 ± 2.64
11013	$\pi^- + p \rightarrow \gamma + n$	C-3	26.72	22.86 ± 3.2

Table 12. Measurement of yield vs magnetic field

Reaction involved	Magnetic Field	Conv.	N_γ	
$\pi^- + p \rightarrow \pi^o + n$	8235	C-2	613,500	Ratio= 0.999 $\pm$ 0.043
$\pi^- + p \rightarrow \pi^o + n$	5538	C-1	614,100	
$\pi^- + p \rightarrow \gamma + n$	8235	C-2	191,400	Ratio= 0.948 $\pm$ 0.041
$\pi^- + p \rightarrow \gamma + n$	11013	C-3	202,000	

Table 13. Panofsky ratio determination

Quantity	Measurement I Value	Measurement II Value
$\frac{N_{d1}}{N_{d2}}$	0.9766 ± 0.0311	2.811 ± 0.112
M	0.935 ± 0.003	1.0
$\frac{\gamma_2(T)}{\gamma_1(T)}$	3.720 ± 0.038	1.147 ± 0.012
$\frac{S_2(T,B)}{S_1(T,B)}$	0.996	1.0
$\frac{\Sigma_2}{\Sigma_1}$	0.947 ± 0.008	1.026 ± 0.013
c_1	0.937	0.939
c_2	0.999	0.999
c_3	0.994	0.994
Panofsky ratio P	1.490 ± 0.050	1.543 ± 0.063

Table 14. Deuterium ratio S determination

Parameter	Value
$\frac{N_{d2}}{N_{d4}}$	1.417 ± 0.039
1+P	2.53 ± 0.02
M	1.204 ± 0.15
$\frac{\gamma_4(T)}{\gamma_2(T)}$	0.995
$\frac{\sum 4}{\sum 2}$	0.970 ± 0.010
S	3.16 ± 0.10

XII. REFERENCES

1. D. W. Joseph, Nuovo Cimento 16, 997 (1960).
2. W.K.H. Panofsky, R. L. Aamodt, and J. Hadley, Phys. Rev. 81, 565 (1951).
3. C. P. Sargent, R. Cornelius, M. Rinehart, L. M. Lederman and K. Rogers, Phys. Rev. 98, 1349 (1955).
4. J. M. Cassels, G. Fidecaro, A. Wetherell, and J. R. Wormald, Proc. Phys. Soc. (London) A70, 405 (1957).
5. J. Fischer, R. March and L. Marshall, Phys. Rev. 109, 533 (1958).
6. J. Kuehner, A. W. Merrison, and S. Tornabene, Proc. Phys. Soc. (London) 73, 545 (1959).
7. L. Koller and A. M. Sachs, Phys. Rev. 116, 760 (1959).
8. M. Derrick, J. Tetkovich, T. Fields and J. Deahl, Phys. Rev. 120, 1022 (1960).
9. N. P. Samios, Phys. Rev. Letters 4, 470 (1960).
10. D. P. Jones, P. G. Murphy, P. L. O'Neill and J. R. Wormald, Proc. Phys. Soc. (London) A77, 77 (1961).
11. V. T. Cocconi, T, Tazzini, G. Fidecaro, M. Legros, N. H. Lipman and A. W. Merrison (submitted for publication in Nuovo Cimento).
12. W. Chinowsky and J. Steinberger, Phys. Rev. 95, 1561 (1954).
13. W. Chinowsky and J. Steinberger, Phys. Rev. 100, 1476 (1955).
14. J. A. Kuehner, A. W. Merrison and S. Tornabene, Proc. Phys. Soc. 73, 551 (1958).
15. H. L. Anderson and E. Fermi, Phys. Rev. 86, 794 (1952).
16. K. A. Brueckner, R. Serber and K. M. Watson, Phys. Rev. 81, 575 (1951).
17. A. S. Wightman, Phys. Rev. 77, 521 (1950); and Ph.D. thesis, Princeton University (1949).
18. J. Fields, G. B. Yodh, M. Derrick and J. Tetkovich, Phys. Rev. Letters 5, 69 (1960).
19. G. A. Snow, University of Maryland, Physics Department, Technical Report, No. 196.
20. J. E. Russell and G. L. Shaw, Phys. Rev. Letters 4, 369 (1960).
21. T. B. Day, G. A. Snow and J. Sucher, University of Maryland, Physics Department, Technical Report No. 159.
22. H. P. Noyes, Phys. Rev. 101, 320 (1956).
23. A. Baldin, Nuovo Cimento 8, 569 (1958).

24. M. Cini, R. Gatto, E. L. Goldwasser and M. Ruderman, Nuovo Cimento 10, 243 (1958).
25. J. Hamilton and W. S. Woolcock, Phys. Rev. 118, 291 (1960).
26. R. Traxler, University of California Physics Department, (private communication).
27. W. P. Swanson, University of California, Lawrence Radiation Laboratory, UCRL-9194.
28. F. S. Crawford and M. L. Stevenson, Phys. Rev. 97, 1305 (1955).
29. R. L. Walker and B. D. McDaniel, Phys. Rev. 74, 315 (1948).
30. K. M. Crowe and R. H. Phillips, Phys. Rev. 96, 470 (1954).
31. L. Landow, J. Phys. (U.S.S.R.) 8, 201 (1944).
32. R. M. Sternheimer, Phys. Rev. 103, 511 (1956).
33. A. M. Hudson, Phys. Rev. 105, 1 (1957).
34. H. Davies, H. A. Bethe and L. C. Maximon, Phys. Rev. 93, 788 (1954).
35. J. A. Wheeler and W. E. Lamb, Phys. Rev. 55, 858 (1939) with correction in Phys. Rev. 101, 1836 (1956).
36. V. Vortruba, Phys. Rev. 73, 1468 (1948).
37. S. Cohen, D. L. Judd and R. L. Riddell, Jr., University of California, Lawrence Radiation Laboratory, UCRL-8391.
38. K. Watson and R. Stuart, Phys. Rev. 82, 738 (1951).
39. R. H. Phillips and K. M. Crowe, Phys. Rev. 96, 484 (1954).
40. H. W. Koch and J. W. Motz, Reviews of Mod. Phys. 31, 920 (1959).